



**CHARACTERIZATION AND  
MEASUREMENTS FROM THE INFRARED  
GRAZING ANGLE REFLECTOMETER**

THESIS

Michael R. Benson, Civilian  
AFIT/OSE/ENP/12-J01

**DEPARTMENT OF THE AIR FORCE  
AIR UNIVERSITY**

***AIR FORCE INSTITUTE OF TECHNOLOGY***

**Wright-Patterson Air Force Base, Ohio**

DISTRIBUTION STATEMENT A

APPROVED FOR PUBLIC RELEASE; DISTRIBUTION UNLIMITED.

The views expressed in this thesis are those of the author and do not reflect the official policy or position of the United States Air Force, Department of Defense, or the United States Government. This material is declared a work of the U.S. Government and is not subject to copyright protection in the United States.

AFIT/OSE/ENP/12-J01

CHARACTERIZATION AND MEASUREMENTS FROM THE INFRARED  
GRAZING ANGLE REFLECTOMETER

THESIS

Presented to the Faculty  
Department of Engineering Physics  
Graduate School of Engineering and Management  
Air Force Institute of Technology  
Air University  
Air Education and Training Command  
in Partial Fulfillment of the Requirements for the  
Degree of Master of Science in Electrical Engineering

Michael R. Benson, BSEE  
Civilian

June 2012

APPROVED FOR PUBLIC RELEASE; DISTRIBUTION UNLIMITED.

AFIT/OSE/ENP/12-J01

CHARACTERIZATION AND MEASUREMENTS FROM THE INFRARED  
GRAZING ANGLE REFLECTOMETER

Michael R. Benson, BSEE  
Civilian

Approved:

---

Michael A. Marciniak, PhD (Chairman)

---

Date

---

Stephen E. Nauyoks, PhD (Member)

---

Date

---

Robert L. Hengehold, PhD (Member)

---

Date

## **Abstract**

A commonly used metric for measuring the reflective properties of a sample is Directional Hemispherical Reflectance (DHR). The Infrared Grazing Angle Reflectometer was specifically designed and built to measure DHR at high angles of incidence. To facilitate this measurement, a novel three dimensional multi-face pyroelectric detector is used. A hemi-ellipsoidal mirror is used to reflect the light scattered by the sample to the detector. The radiometric model for this system is derived and simulated to illustrate that this detector can theoretically measure better than 98% of the light reflected by the sample, regardless of the diffusivity of the sample measured. This error is shown to be angularly dependent, and cannot be calibrated out of the measurement. The setup of this equipment, as well as the modifications implemented at AFIT, is discussed, and the procedure for calibration is derived. Finally, several sample measurements and the associated difficulties are discussed.

## Acknowledgements

To Dr. Marciniak, who gave me an opportunity I did not deserve.

To all of my professors, who taught me everything I know.

To my coworkers, who helped me work through all of this.

To my friends and my family and my friends who are my family, who been by my side this entire time.

To my Dad, who always knew I could do better.

To my Mom, who will always be smarter than me.

To my God, who gave me all of these.

Thank you so much.

Michael R. Benson

# Table of Contents

	Page
Abstract .....	iv
Acknowledgements .....	v
List of Figures .....	viii
List of Tables .....	x
List of Symbols .....	xi
List of Abbreviations .....	xii
I. Introduction .....	1
1.1 Overview .....	2
1.2 Axis and Units .....	3
II. Discussion of DHR .....	4
III. Detector Theory .....	7
3.1 Sample Power at the Detector .....	7
3.2 Simulating Large Samples .....	14
IV. Non-Ideal Detector Faces .....	19
4.1 Detector Absorption .....	19
4.2 Samples .....	21
4.3 Interpreting Results .....	25
4.4 Simulation Parameters .....	25
4.5 Results .....	26
4.6 Summary .....	29
V. Measurement Theory .....	31
5.1 Basic DHR Measurements .....	31
5.2 Calculating $C_d$ and $C_w$ .....	32
5.3 Atmospheric Effects .....	33
5.4 Calibration .....	35
5.5 Making Measurements .....	36
5.6 Uncertainty .....	38
5.7 IGAR Algorithm .....	40
5.8 Summary .....	41

	Page
VI. Equipment Description .....	42
6.1 Theory of Operation .....	42
6.2 Hardware .....	42
6.3 Alignment .....	47
6.4 Calibration .....	50
6.5 Software .....	53
VII. Algorithms .....	54
7.1 Laser Autotuning Algorithm .....	54
7.2 IGAR Algorithm .....	56
VIII. Measurements .....	58
8.1 Aluminum Block .....	58
8.2 Gold Mirror .....	59
8.3 Experimental Results .....	61
IX. Conclusions and Future Work .....	63
9.1 Conclusions .....	63
A. Measurement Uncertainty Expanded .....	64
B. MATLAB Code .....	66
2.1 cookTorrance.m .....	66
2.2 cookTorranceVL.m .....	68
2.3 detectorOptimal3.m .....	70
Bibliography .....	77
Vita .....	79



## List of Figures

Figure		Page
1.	Axis used for this paper.....	3
2.	Pictorial depiction of DHR.....	5
3.	The ellipsoidal mirror images the detector into object space around the sample.....	9
4.	Image of the detector .....	9
5.	Top face of the detector imaged into object space .....	11
6.	Front face of the detector imaged into object space .....	13
7.	Definition of the vector V .....	16
8.	Sample scatter patterns .....	24
9.	Actual and Detected DHR for the Black Oxidized Steel scatterer.....	28
10.	Actual and Detected DHR for the Acrylic Blue scatterer .....	28
11.	Actual and Detected DHR for the Gold Metallic scatterer .....	29
12.	IGAR diagram .....	43
13.	Photograph of IGAR .....	43
14.	Optical train used in IGAR .....	45
15.	Diagram of the detector .....	46
16.	$x$ angular and positional misalignment. ....	47
17.	$y$ angular misalignment. ....	48
18.	$y$ positional misalignment. ....	48
19.	$x$ positional misalignment at normal incidence and at $70^\circ$ .....	49
20.	Laser Autotuning Algorithm .....	55
21.	IGAR Algorithm .....	57

Figure		Page
22.	The DHR and face voltages for the rough surfaced aluminum block. ....	59
23.	Simulated measurements using the Black Oxidized Steel scatterer compared to the measurements of the aluminum block .....	60
24.	The DHR and face voltages for the gold calibration mirror. ....	61
25.	Simulated measurements using the Gold Metallic scatterer compared to the measurements of gold calibration mirror .....	62

## List of Tables

Table		Page
1.	List of the index $j$ and it's associated face. ....	16
2.	List of the index $j$ and the information associated with the summation for calculating $\Phi_j$ .....	18
3.	List of sample scatter pattern fitting values. All values were taken from Ngan's paper "Experimental Analysis of BRDF Models - Supplemental" [1]. ....	24
4.	Relevant values for the simulation. ....	26

## List of Symbols

Symbol		Page
$\rho$	Directional Hemispheric Reflectance .....	4
$\Omega$	Solid Angle .....	4
$\Phi$	Radiant Flux .....	4
$f_r$	Bidirectional Reflective Distribution Function .....	4
$L$	Radiance .....	10
$A$	Area .....	10
$r$	radius .....	10

## List of Abbreviations

Abbreviation		Page
DHR	Directional Hemispherical Reflectance . . . . .	4
BRDF	Bidirectional Reflectance Distribution Function . . . . .	4
HDR	Hemispherical Directional Reflectance . . . . .	5
QCL	Quantum Cascade Laser . . . . .	44

# CHARACTERIZATION AND MEASUREMENTS FROM THE INFRARED GRAZING ANGLE REFLECTOMETER

## I. Introduction

During November of 2011, the Air Force Research Lab received a new piece of equipment from Northrop Grumman Corporation. The Infrared Grazing Angle Reflectometer is a piece of equipment designed to analyze samples and report back their Directional Hemispheric Reflectance. This material property is a widely used metric in the United States Air Force to describe how much light is reflected off a sample at a given angle of incidence. A sample's DHR is used in many different ways, ranging from modeling the infrared signature of fighter jets to calculating how much the absorbance of a material. IGAR quickly and accurately calculates this value for a sample for a wide range of incident angles, increasing the measurement capabilities of the Air Force of the United States.

DHR is a ratio of the power reflected by a surface over the power incident on that surface. Making measurements of the power reflected over such a large area is a difficult problem. To make this measurement, Northrop Grumman used a ellipsoidal hemispherical mirror to collect the light, and focus it to a detector. Because of the angles involved in the measurement, a novel five sided pyroelectric detector was created to measure this reflected light. In order to prove that we can make accurate measurements of the DHR of the sample, we must first prove that we can properly measure this reflected power using this detector.

An ideal detector can measure all of the light incident upon it. For an actual detector, this is not the case. For most systems, we collect light at only a single

angle of incidence, meaning that this inefficiency is a constant, and can be calibrated out of the system. However, for this system, we collect light over a range of angles. Because the ability for the detector to absorb light varies as a function of angle, we can't calibrate this inefficiency out of the system. However, as is shown later, this inefficiency is minor, and can in most cases be ignored.

In order to use the detector to make DHR measurements, a robust calibration system is needed. This calibration system is derived and discussed for this system. By using mirrors with known reflectivities, we can calibrate all five sides of the detector, and make accurate DHR measurements of the sample. Some of these measurements are compared to their theoretical counterparts.

## 1.1 Overview

The most important piece of IGAR is the detector used in measurements. In order to understand how the detector makes measurements, the theory behind the detector needs to be understood, which motivates Chapter III, Detector Theory. This section makes two critical assumptions in the operation of the detector, which are not true in practice. Chapter IV, Non-Ideal Detector Faces, addresses both of these assumptions, and provides several simulations to examine how well the this detector can detect light.

Chapter V, Measurement Theory, examines how this detector can be used in the IGAR system to measure the DHR of a sample. This chapter serves as the bridge between the theory of the operation of IGAR and implementing this system in a laboratory setting. Actually implementing this system is covered in Chapter VI, Equipment Description. Chapter VII two of the most important pieces of software used in the previous chapter. Finally, Chapter VIII, examines some of the measurements made by this system, and compares them conceptually to the simulations

performed earlier.

## 1.2 Axis and Units

The axis shown in Figure 1 will be used throughout the rest of the document.  $\theta$  refers to the polar angle between a vector and the  $\hat{z}$  axis.  $\phi$  is the azimuthal angle, measured from the  $\hat{x}$  axis to the projection of the vector into the  $xy$  plane. For example, a vector with  $\theta = 0^\circ$  would be parallel to the normal vector, and a vector with  $\theta = 90^\circ$  would be perpendicular to the normal.

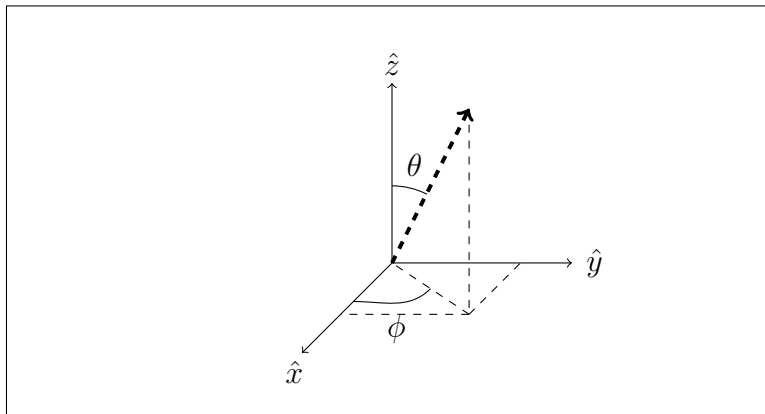


**Figure 1. Axis used for this paper.**

The SI units of measure are used throughout the entire document. Most distances measured are relatively short, making millimeters the preferred unit of distance. This makes millimeters-squared the natural unit for area. Angles will be defined in either radians or degrees. Radians are the preferred unit of measure in Chapter III, due to the mathematics involved in the calculations. Throughout the rest of the document, degrees are used.

All power measurements are reported in watts. Wavelengths will be measured in microns. DHR measurements are unitless, and BRDF measurements have units of inverse steradians.



## II. Discussion of DHR

Directional Hemispherical Reflectance (DHR) is a measure of the ratio between the light incident and the light reflected off a surface for a single angle of incidence [18]. Nicodemus defined this relationship as the flux seen looking at the surface over the flux incident:

$$\rho(\Omega_i; \Omega_r) = \frac{d\Phi_r}{d\Phi_i}, \quad (1)$$

where  $\rho$  is the DHR of the surface in question,  $\Omega$  is a solid angle, the subscripts  $i$  and  $r$  refer to incident and reflected radiation respectively, and  $\Phi$  is the radiant flux. This is depicted in Figure 2. In practice,  $\Omega_r$  typically refers to the entire hemisphere of reflectance, making DHR a function of only angle of incidence. The majority of samples are isotropic, meaning that this measure can be defined only as a function of angle of incidence in a single plane. Samples without this symmetry must be defined for both this angle of incidence and the orientation of the sample. It is important to note that several other variables can be added to this equation, taking into account such effects as sample temperature, input polarization or wavelength. These effects will be ignored throughout the paper, and DHR will only be talked about as a function of angle of incidence in a single plane.

DHR can be expressed in terms of Bidirectional Reflectance Distribution Function (BRDF) [18],

$$\rho(\omega_i; 2\pi) = \frac{\int_{2\pi} \int_{\omega_i} f_r(\theta_i, \phi_i; \theta_r, \phi_r) L_i(\theta_i, \phi_i) d\Omega_i d\Omega_r}{\int_{\omega_i} L_i(\theta_i, \phi_i) d\Omega_i} \quad (2)$$

where  $f_r$  is the BRDF of the material. According to Nicodemus [18], if we assume a uniform and isotropic incident beam, and take the wavelength into account, we can

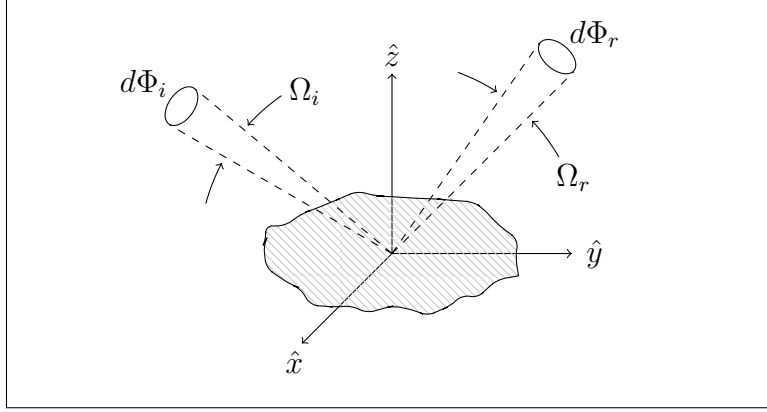


**Figure 2.** Picture of DHR from Nicodemus paper. Note that, in the rest of this paper, DHR refers to the light reflected over the entire hemisphere, not some portion  $\omega_r$ .

rewrite the equation as

$$\rho(\theta_i, \phi_i; \lambda) = \int_0^{\pi/2} \int_0^{2\pi} f_r(\theta_r, \phi_r; \theta_i \phi_i; \lambda) \cos \theta_r \sin \theta_r d\phi_r d\theta_r. \quad (3)$$

Note that while this equation shows a clear path between BRDF and DHR, this calculation is non-trivial given real data. The majority of measured BRDF data is measured for only a single value of  $\phi_r$ . In order to actually calculate the integral, the value of the BRDF for all other values of  $\theta_r$  have to be calculated. Circular symmetry around the incident beam is a good assumption, but very difficult to calculate due to the geometry involved. There are very few practical ways to go between measured BRDF and DHR data. Balling did make this conversion in his research [2], but only for  $\theta_i = 0$ . The angle of incidence he chose made the geometry of the problem much easier.

As a note, DHR and Hemispherical Directional Reflectance (HDR) are the same information measured in different ways [13]. In a DHR measurement, the sample is illuminated from a single angle, and the signal is integrated over all angles. In HDR, the sample is illuminated from all directions, typically using a blackbody and

hemi-ellipsoid mirror, and the signal is measured from a single angle. The SOC-100, manufactured by Surface Optics Corp., San Diego, CA, is an example of an instrument which operates in this manner. By reciprocity, both of these measurements yield the same information. One of the biggest advantages of this piece of equipment is the ability to measure the spectral characteristics of the sample. Because the sample is illuminated by a blackbody, the instrument can measure a broad range of wavelengths simultaneously. However, the directional emittance of the blackbody limits the angular capabilities of the measurement, necessitating the use of laser sources in a grazing angle instrument.

### III. Detector Theory

The purpose of this section is to prove that the total power emitted by the sample can be measured by this detector. In this experiment, a laser is used to illuminate a sample, which is located at the bottom focus of a hemi-ellipsoidal mirror. The light reflected by the sample is scattered onto an mirror, and reflected to the second focus where a detector has been mounted. This detector is particularly novel, as it is a five sided pyroelectric detector. The goal of this chapter is to show that the total power emitted by the sample is equal to the sum of the power detected by each side of the detector.

Initially, two critical assumptions are made. The first assumption is that the distance from the sample to the detector doesn't change over the size of the of the sample. This greatly simplifies the problem and allows a closed form solution to the calculation. In general, this is not true, and will be addressed in Section ???. The second assumption is that the detector is a perfect detector and can perfectly detect all light incident upon it. This is also not true, and can easily be addressed after redefining the problem to address the previous assumption. By making these two assumptions, a closed form solution to the problem can be calculated and compared to the ideal case, showing that, in the best case scenario, this detector can properly measure the power reflected by the sample.

#### 3.1 Sample Power at the Detector

In order to prove that the total power reflected by the sample can be calculated by summing the power seen by each side of the detector, the power seen by each side of the detector must be calculated. Using the relationship between power and radiance, the power incident on each side of the detector can easily be calculated

given any particular scatter pattern. Assuming that the total power is equal to the power collected by each face of the detector, the sum of all five faces should be equal to the total power emitted by the sample.

As stated before, the experiment is constructed such that the sample and detector are placed at opposite foci of an hemi-ellipsoidal mirror. An ellipsoidal mirror is constructed in such a way that any ray leaving the first focus will be reflected to the second focus [10]. This means that the detector is essentially imaged at the sample. Every ray leaving the sample will be reflected from the mirror towards the detector. A depiction of the imaged detector can be seen in Figure 3.

It is important to note that this theoretical description of the system assumes that, from the point of view of these radiometric calculations, the image of the detector is a perfect image. In practice, this is not true. The hemi-ellipsoidal mirror deforms each face of the detector into a curved shape. This new shape is very difficult to analyze analytically, necessitating the use of the perfect image assumption. The small size of the detector relative to the radii of the hemi-ellipsoidal mirror make this deformation minor and this assumption holds true. Our future research is going to examine the effects of accounting for the deformation of the image of the detector caused by the mirror. With the deformed image, the same analysis can then be applied to the system.

Because of the setup of this experiment, the system can be approximated as an emitter which emits light in the same way that the sample would reflect it. The mirror will create a 1:1 image of the detector in object space, which means the system can be modeled as if the detector was built around the sample. Note that this approach ignores complications such as mirror aberrations and imperfections. To account for these effects, an optics modeling package such as Zemax would be needed. The image of the detector with the associated dimensions can be seen in Figure 4.

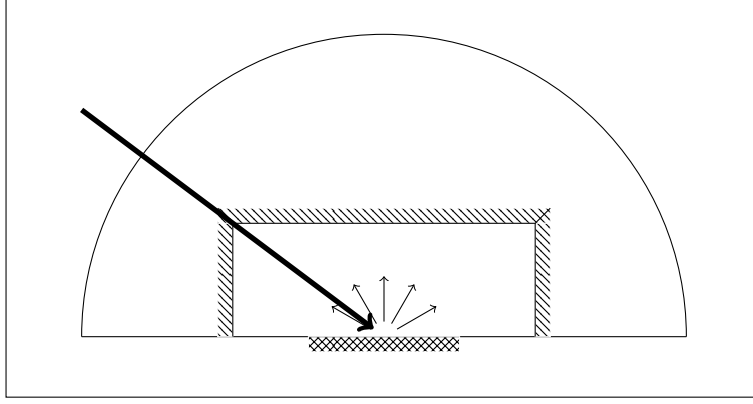


**Figure 3.** The ellipsoidal mirror essentially images the detector into object space around the sample. Assuming the sample is very small, the detector can be analyzed as if it is being illuminated by a point source located at the foci of the mirror.

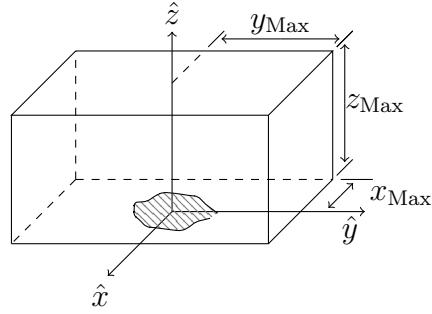


**Figure 4.** This is a diagram of the image of the detector. The face perpendicular to the  $x$  axis is the Left Face, the one perpendicular to the  $y$  axis is the Front Face, and the one perpendicular to the  $z$  axis is the Top Face.

This system can be modeled as a system with a very small sample located at the focal point of the mirror. Specifically, the sample must be small enough that the distance from the sample to the detector doesn't change over the area of the sample. Initially, a Lambertian scatterer will be analyzed. This scatterer has the simplest definition, simplifying the problem and enabling a closed form solution. Later, a simulation will be used to analyze different scatter patterns. For this sample, the energy radiated from it can be calculated from the equation

$$\partial^2 \Phi = L_0 \cos \theta_d \partial A_s \partial \Omega_d \quad (4)$$

where  $\Phi$  is the total power,  $L_0$  is some constant radiance,  $A_s$  is the area of the emitter, and  $\Omega_d$  is the solid angle in which power is emitted [8]. To calculate the total power emitted, we need to integrate over both the area of the emitter and the solid angle. Integrating the above equation over the area of the detector yields

$$\partial\Phi = A_s \int_{\Omega_s} L_0 \cos \theta \partial\Omega_d. \quad (5)$$

$\partial\Omega_d$  can be defined in terms of  $\phi_d$  and  $\theta_d$ :

$$\partial\Omega_d = \sin \theta_d d\phi_d d\theta_d, \quad (6)$$

which makes (5)

$$\Phi_{\text{Optimal}} = A_s \int_0^{2\pi} \int_0^{\pi/2} L_0 \cos \phi_d \sin \phi_d d\theta_d d\phi_d = \pi A_s L_0. \quad (7)$$

This result is the power emitted by a perfectly Lambertian scatterer.

Now, in order to calculate the total power detected by the detector, the power seen by each face must be calculated. (5) is an ideal starting point, but integrating over angle space is difficult. Instead a rectangular face located a distance away from the detector can be used instead of integrating over all possible angles, as seen in Figure 5.

Now,  $\partial\Omega_d$  will be redefined as

$$\partial\Omega_d = \frac{dx_d dy_d}{r^2} \cos \alpha \quad (8)$$

where  $r$  is the distance from the center of the sample to the center of the differential area.  $\cos \alpha$  is the angle between the normal of the differential area and the ray going from the differential area to the sample. Since this face is parallel to the sample, the

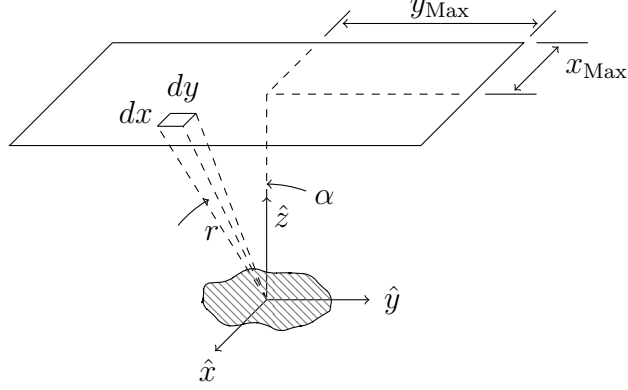


**Figure 5. The top face is essentially imaged upside down into object space. An ellipsoidal mirror makes a 1:1 image of the object, meaning that the image of the detector has the same dimensions as the object.**

angle  $\alpha$  is the same as the angle  $\theta_d$ .  $r$  is the distance from our sample (located at  $(0,0,0)$ ), which makes the differential solid angle

$$\partial\Omega_d = \frac{dx_d dy_d}{x_d^2 + y_d^2 + z_d^2} \cos \theta_d \quad (9)$$

Since this face faces  $-\hat{z}$ , this cosine term becomes  $\frac{z_d}{r}$ . Now, instead of integrating over angle space, we can integrate over  $(x_d, y_d, z_d)$  space.

$$\Phi_{\text{Top}} = A_s \int_{y_{\text{Min}}}^{y_{\text{Max}}} \int_{x_{\text{Min}}}^{x_{\text{Max}}} L_0 \cos \theta_d \frac{dx_d dy_d}{x_d^2 + y_d^2 + z_d^2} \cos \theta_d. \quad (10)$$

We choose to convert  $\cos \theta_d$  to cartesian space to simplify the integration.

$$\cos \theta_d = \frac{z_d}{r} = \frac{z_d}{\sqrt{x_d^2 + y_d^2 + z_d^2}} \quad (11)$$

which makes the previous equation

$$\Phi_{\text{Top}} = A_s \int_{y_{\text{Min}}}^{y_{\text{Max}}} \int_{x_{\text{Min}}}^{x_{\text{Max}}} L_0 \frac{z^2}{(\sqrt{x^2 + y^2 + z^2})^2} dx dy. \quad (12)$$



For simplicity, a detector symmetric about the axis is assume, making  $x_{\text{Min}} = -x_{\text{Max}}$  and  $y_{\text{Min}} = -y_{\text{Max}}$ .  $z$  is a constant over the surface, and is equal to  $z_{\text{Max}}$ . Completing the integration reveals

$$\Phi_{\text{Top}} = A_s L_0 \left[ \frac{2x_{\text{Max}}}{\sqrt{x_{\text{Max}}^2 + z_{\text{Max}}^2}} \tan^{-1} \left( \frac{y_{\text{Max}}}{\sqrt{x_{\text{Max}}^2 + z_{\text{Max}}^2}} \right) + \frac{2y_{\text{Max}}}{\sqrt{y_{\text{Max}}^2 + z_{\text{Max}}^2}} \tan^{-1} \left( \frac{x_{\text{Max}}}{\sqrt{y_{\text{Max}}^2 + z_{\text{Max}}^2}} \right) \right]. \quad (13)$$

Making both  $x_{\text{Max}}$  and  $y_{\text{Max}} \gg z_{\text{Max}}$  gives

$$\begin{aligned} \Phi_{\text{Top}} &= A_s L_0 \left[ \frac{2x_{\text{Max}}}{\sqrt{x_{\text{Max}}^2}} \tan^{-1} \left( \frac{y_{\text{Max}}}{\sqrt{x_{\text{Max}}^2}} \right) + \frac{2x_{\text{Max}}}{\sqrt{y_{\text{Max}}^2}} \tan^{-1} \left( \frac{x_{\text{Max}}}{\sqrt{y_{\text{Max}}^2}} \right) \right] \\ &= A_s L_0 \left[ 2 \tan^{-1} \left( \frac{y_{\text{Max}}}{\sqrt{x_{\text{Max}}^2}} \right) + \pi - 2 \tan^{-1} \left( \frac{y_{\text{Max}}}{\sqrt{x_{\text{Max}}^2}} \right) \right] = \pi A_s L_0, \end{aligned} \quad (14)$$

which is what we would expect for a Lambertian source.

Now, for the sides of the detector. The first face to be analyzed will be the front face of the detector ( $y_d$  is held constant). This is depicted in Figure 6. By symmetry, the back is the same as the front. By extension, the left is the same as the front with  $x_{\text{Max}}$  and  $y_{\text{Max}}$  exchanged.

(5) is again used as a starting point. The same transition from angular space to cartesian space is used.

$$\partial\Omega_d = \frac{dx_d dz_d}{r^2} \cos \alpha \quad (15)$$

where  $r$  is defined the same as above. Because the face points in the  $-\hat{y}$  direction,  $\cos \alpha$  becomes  $y_d/r$ :

$$\cos \alpha = \frac{y_d}{r} = \frac{y_d}{\sqrt{x_d^2 + y_d^2 + z_d^2}}. \quad (16)$$

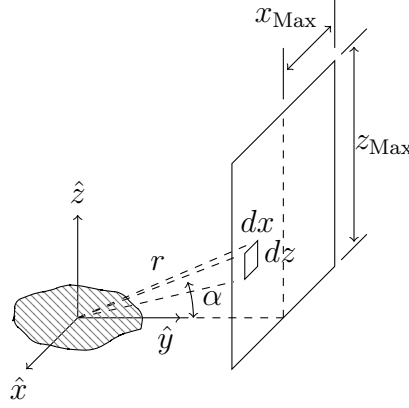


**Figure 6.** The front of the detector is imaged in the same fashion as the top. See the caption associated with Figure 5.

This makes

$$\partial\Omega_d = \frac{y_d \, dx_d \, dz_d}{(\sqrt{x_d^2 + y_d^2 + z_d^2})^3}. \quad (17)$$

$\cos\theta$  has the same value as above. Therefore,

$$\Phi_{\text{Front}} = A_s L_0 \int_{x_{\text{Min}}}^{x_{\text{Max}}} \int_0^{z_{\text{Max}}} \frac{z_d}{\sqrt{x_d^2 + y_d^2 + z_d^2}} \frac{y_d}{(\sqrt{x_d^2 + y_d^2 + z_d^2})^3} dz_d \, dx_d. \quad (18)$$

This time,  $y_d$  will be held constant at  $y_{\text{Max}}$ .  $x_{\text{Min}} = -x_{\text{Max}}$ , making

$$\Phi_{\text{Front}} = A_s L_0 \left[ \tan^{-1} \left( \frac{x_{\text{Max}}}{y_{\text{Max}}} \right) - \frac{y_{\text{Max}}}{\sqrt{y_{\text{Max}}^2 + z_{\text{Max}}^2}} \tan^{-1} \left( \frac{x_{\text{Max}}}{\sqrt{y_{\text{Max}}^2 + z_{\text{Max}}^2}} \right) \right]. \quad (19)$$

The same line of reasoning can be used to calculate the power seen by the left face of the detector. The only difference is this time,  $x$  will be held constant, and integration occurs over  $y$ . The net effect on this is that  $\Phi_{\text{Left}}$  has the same form as  $\Phi_{\text{Front}}$ , only with  $x_{\text{Max}}$  and  $y_{\text{Max}}$  exchanged.

$$\Phi_{\text{Left}} = A_s L_0 \left[ \tan^{-1} \left( \frac{y_{\text{Max}}}{x_{\text{Max}}} \right) - \frac{x_{\text{Max}}}{\sqrt{x_{\text{Max}}^2 + z_{\text{Max}}^2}} \tan^{-1} \left( \frac{y_{\text{Max}}}{\sqrt{x_{\text{Max}}^2 + z_{\text{Max}}^2}} \right) \right]. \quad (20)$$

Earlier, the claim was made that the total power reflected by the sample was equal

to the sum of power seen by each face of the detector. This sum of powers would be equal to the ideal case, which is  $\pi A_s L_0$ .

$$\Phi_\Sigma = \Phi_{\text{Top}} + \Phi_{\text{Left}} + \Phi_{\text{Front}} + \Phi_{\text{Right}} + \Phi_{\text{Back}} \quad (21)$$

Due to the symmetry of the detector,  $\Phi_{\text{Right}} = \Phi_{\text{Left}}$  and  $\Phi_{\text{Back}} = \Phi_{\text{Front}}$ . This makes the above equation

$$\Phi_\Sigma = \Phi_{\text{Top}} + 2\Phi_{\text{Left}} + 2\Phi_{\text{Front}} \quad (22)$$

Inserting the equations calculated above for these terms, the two terms of  $\Phi_{\text{Top}}$  cancel out the second portion of both  $2\Phi_{\text{Left}}$  and  $2\Phi_{\text{Front}}$ , leaving

$$\Phi_\Sigma = A_s L_0 \left[ 2 \tan^{-1} \left( \frac{x_{\text{Max}}}{y_{\text{Max}}} \right) + 2 \tan^{-1} \left( \frac{y_{\text{Max}}}{x_{\text{Max}}} \right) \right]. \quad (23)$$

Defining a new arbitrary angle  $\beta$  to be equal to  $\tan^{-1}(x_{\text{Max}}/y_{\text{Max}})$ . It follows then that  $\pi/2 - \beta = \tan^{-1}(y_{\text{Max}}/x_{\text{Max}})$ , making the above equation

$$\Phi_\Sigma = A_s L_0 [2\beta - 2\beta + 2\pi/2] = \pi A_s L_0. \quad (24)$$

In (7), this is shown to be the total power emitted by the sample. Therefore, by summing the power seen on each side of the detector, the detector can capture the total power emitted by the sample.

### 3.2 Simulating Large Samples

There were two critical assumptions made in the above section. The first is that the sample is significantly smaller than the detector. This allowed the formula for calculating the distance from the sample to the detector to be greatly simplified, which makes the analytic solution possible. In general, this is not the case. From

a design perspective, the detector should be as small as possible, which means the radius distance will vary significantly from one side of the sample to the other. The other assumption made was that the detector can absorb all of the light incident upon it, which will be addressed in the following section.

Both of these assumptions are what enabled a closed form solution for the power seen by the detector. Now, with the added complexity of the system, a numeric solution is the preferred solution to this problem. To facilitate this, (4) can be rewritten as

$$\Delta^2\Phi = L(\theta_s, \phi_s) \cos \theta_s \Delta\Omega_d \Delta A_s \quad (25)$$

Each face needs to be treated separately from the other, so we actually need to calculate this power five different times. We will use the subscript  $j$  to indicate which face we are dealing with. A list of the index  $j$  and its associated face can be found in Table 1. This makes equation (25)

$$\Delta^2\Phi_j = L(\theta_s, \phi_s) \cos \theta_s \Delta\Omega_{d,j} \Delta A_s. \quad (26)$$

We can rewrite  $\Delta\Omega_{d,j}$  as

$$\Delta\Omega_{d,j} = \frac{\Delta A_{d,j}}{r^2(\Delta A_s, \Delta A_d)} \cos \theta_d. \quad (27)$$

which makes (26)

$$\Delta^2\Phi = L(\theta_s, \phi_s) \cos \theta_s \cos \theta_d \frac{1}{r^2(\Delta A_d, \Delta A_s)} \Delta A_d \Delta A_s \quad (28)$$

which says that the differential power is a function of both the position of the differential area of the sample and the position of the differential area of the detector.

To make the calculations of  $r(\Delta A_s, \Delta A_d)$  and  $\cos \theta$  easier, we will now define the

**Table 1. List of the index  $j$  and it's associated face.**

$j$	= 1: Front
	= 2: Left
	= 3: Back
	= 4: Right
	= 5: Top

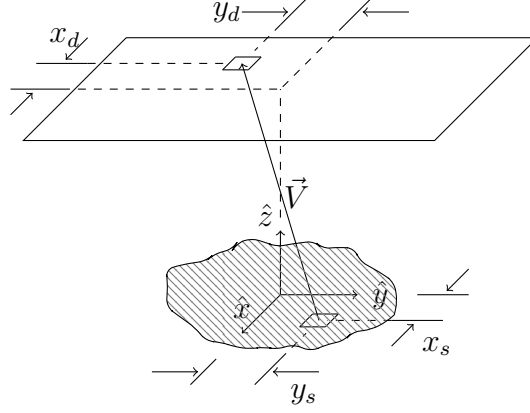


**Figure 7. The vector  $\vec{V}$  is the vector starting at the differential area of the sample and ending at the differential area of the detector.**

vector  $\vec{V}$  as the vector starting at the differential area of the sample and ending at the differential area of the detector, as shown in Figure 7.

$$\vec{V}(\Delta A_d, \Delta A_s) = \vec{V}(x_s, y_s; x_d, y_d, z_d) = (x_d - x_s)\hat{x} + (y_d - y_s)\hat{y} + (z_d)\hat{z} \quad (29)$$

where the  $s$  subscript represents the position on the sample, and the  $d$  subscript represents the position on the detector. Now, the distance  $r$  is just the length of the vector  $\vec{V}$ . (Note: At this point, the  $(\Delta A_d, \Delta A_s)$  portion of the  $\vec{V}$  term will be omitted for brevity.)

$$r(\Delta A_d, \Delta A_s) = ||\vec{V}|| = \sqrt{(x_d - x_s)^2 + (y_d - y_s)^2 + z_d^2}, \quad (30)$$

The term  $\cos \theta_s$  can now be written as

$$\cos \theta_s = \frac{\vec{V} \cdot \hat{z}}{\|\vec{V}\|} = \frac{z_d}{\|\vec{V}\|}. \quad (31)$$

$\cos \theta_{d,j}$  now becomes

$$\cos \theta_{d,j} = \frac{\vec{V} \cdot \hat{n}_j}{\|\vec{V}\|}, \quad (32)$$

where  $\hat{n}$  is the normal vector for the face of the detector.

In order to calculate the power incident on each face of the detector, we need to apply a summation to (28).

$$\Phi_j = \sum_{A_s} \sum_{A_{d,j}} L(\theta_{d,j}, \phi_{d,j}) \frac{\vec{V} \cdot \hat{z}}{\|\vec{V}\|} \frac{\vec{V} \cdot \hat{n}_j}{\|\vec{V}\|} \frac{1}{\|\vec{V}\|^2} \Delta A_{d,j} \Delta A_e. \quad (33)$$

where  $A_s$  is the area of the sample,  $\Delta A_s$  is the differential area of the sample,  $A_{d,j}$  is the area of the  $j^{\text{th}}$  detector face, and  $\Delta A_{d,j}$  is the differential of that area.

$A_s$  is the range of  $x$  values from  $-x_{s,\max} : x_{s,\max}$  with a step size of  $\Delta x_s$ , and the  $y$  values from  $-y_{s,\max} : y_{s,\max}$  with a step size of  $\Delta y_s$ . The range of  $A_{d,j}$  and the value of  $\Delta A_{d,j}$  are defined in Table 2. This formula still assumes a perfect detector which can detect all of the light incident upon it.

As shown in (21), the total power is equal to the sum of the power detected by each face of the detector. This makes the total power of the detector

$$\Phi_{\text{act}} = \sum_j \Phi_j. \quad (34)$$

Performing this calculation for an arbitrary detector and sample geometry gives results very close to the optimal result of  $\Phi_{\text{det}} = \pi A_s L_0$ . These results show that this detector can still recover all of the power emitted by the sample, which is what is expected given the results from the previous section.

**Table 2.** List of the index  $j$  and the information associated with the summation for calculating  $\Phi_j$ .

Front:	$A_{d,1} = \{y_d = -y_{\max} : y_{\max}, z_d = 0 : z_{\max}\}$	$x_d = x_{\max}$
	$\Delta A_{d,1} = \Delta y_d \Delta z_d$	$\hat{n}_1 = -\hat{x}$
Left:	$A_{d,2} = \{x_d = -x_{\max} : x_{\max}, z_d = 0 : z_{\max}\}$	$y_d = y_{\max}$
	$\Delta A_{d,2} = \Delta x_d \Delta z_d$	$\hat{n}_2 = -\hat{y}$
Back:	$A_{d,3} = \{y_d = -y_{\max} : y_{\max}, z_d = 0 : z_{\max}\}$	$x_d = -x_{\max}$
	$\Delta A_{d,3} = \Delta y_d \Delta z_d$	$\hat{n}_3 = \hat{x}$
Right:	$A_{d,4} = \{x_d = -x_{\max} : x_{\max}, z_d = 0 : z_{\max}\}$	$y_d = -y_{\max}$
	$\Delta A_{d,4} = \Delta x_d \Delta z_d$	$\hat{n}_4 = \hat{y}$
Top:	$A_{d,5} = \{x_d = -x_{\max} : x_{\max}, y_d = -y_{\max} : y_{\max}\}$	$z_d = z_{\max}$
	$\Delta A_{d,5} = \Delta x_d \Delta y_d$	$\hat{n}_5 = -\hat{z}$

Now, the equation (33) addresses the first assumption made in the previous section. This equation assumes a large sample, yet shows that the detector can still detect all of the light scattered by the sample. This new framework can be easily extended to address the second assumption that was made earlier. The vector  $\vec{V}$  enables us to implement an angle dependent absorption function on each face of the detector, addressing the fact that no real detector is a perfect absorber.

## IV. Non-Ideal Detector Faces

In Chapter III, where the general solution for the power seen by the detector was derived, there were two variables which were undefined. The first was  $L(\vec{V})$ , which is the radiance seen by the differential area of the detector. The second was  $\alpha(\vec{V})$ , which is the absorptance experienced by that same area. The radiance can be defined very well using a BRDF model, and the absorptance can be modeled using a Fresnel absorptance. After defining both of these values, we can calculate the power seen by the detector, and analyze it's behavior.

### 4.1 Detector Absorption

The second assumption that was previously made is that the detector can absorb all of the incident light. This is not true. While dark materials absorb most energy, some of the light is reflected. This implies that the absorptivity of the detector is a function of angle, which drastically complicates the calculation of power. Ideally, this calculation would be performed with a BRDF model of the face of the detector. This paper will examine the case of a flat detector with some index of refraction  $n$ . This air-detector interaction will result in a Fresnel reflection, from which the absorption of the detector can be calculated.

The Fresnel reflection of the detector face is composed of two terms: one for the  $S$  polarized light and one for the  $P$  polarized light [4]. Both of these terms can be calculated as a function of the angle of incidence  $\theta_i$  and the index of refraction of the



detector,  $n$ . (It is assumed that the index of refraction of the air is 1.)

$$R_S(n, \theta_i) = \left| \frac{\cos \theta_i - n \sqrt{1 - \frac{1}{n^2} \sin^2 \theta_i}}{\cos \theta_i + n \sqrt{1 - \frac{1}{n^2} \sin^2 \theta_i}} \right|^2 \quad (35)$$

$$R_P(n, \theta_i) = \left| \frac{\sqrt{1 - \frac{1}{n^2} \sin^2 \theta_i} - n \cos \theta_i}{\sqrt{1 - \frac{1}{n^2} \sin^2 \theta_i} + n \cos \theta_i} \right|^2 \quad (36)$$

If the assumption that the light reflected by the sample is randomly polarized is made, the reflectance of the detector face will be

$$R(n, \theta_i) = \frac{R_S(n, \theta_i) + R_P(n, \theta_i)}{2}. \quad (37)$$

Using Kirchoff's Law [14], the absorption of the face is equal to one minus the reflection. Therefore, the absorption of the detector face can be expressed as

$$\alpha(n, \theta_i) = 1 - R(n, \theta_i). \quad (38)$$

Note that the above equation defines  $\alpha$  in terms of  $\theta_i$ . For this detector, the angle  $\theta_i$  is equal to the angle between the differential area of the detector and the differential area of the sample, which is  $\theta_{d,j}$ . Using (38), this angle can be calculated for any vector  $\vec{V}$ , allowing (38) to be expressed as

$$\alpha(\vec{V}, n) = 1 - R(\vec{V}, n). \quad (39)$$

Now, (33) can be rewritten to account for the absorptivity of the detector.

$$\Delta^2 \Phi_j = L(\theta_{d,j}, \phi) \alpha(\vec{V}, n) \frac{(\vec{V} \cdot \hat{z})(\vec{V} \cdot \hat{n}_j)}{\|\vec{V}\|^4} \Delta A_{d,j} \Delta A_e. \quad (40)$$

Applying the same summation as before,

$$\Phi_j = \sum_{A_s} \sum_{A_{d,j}} L(\theta_{d,j}, \phi) \alpha(\vec{V}, n) \frac{(\vec{V} \cdot \hat{z})(\vec{V} \cdot \hat{n}_j)}{||\vec{V}||^4} \Delta A_{d,j} \Delta A_e. \quad (41)$$

If  $\alpha(\vec{V}, n)$  was a constant, it could be factored out of the summation, and could be corrected by using a compensation term. However, it is a function of the vector  $\vec{V}$ , which means that information is lost, and cannot be corrected. Once again, the total power seen by the detector is simply the sum of the powers seen by each face of the detector, or

$$\Phi_{\text{det}} = \sum_j \Phi_j. \quad (42)$$

## 4.2 Samples

Now, the only thing left to define in (41) is the radiance of the sample. We can easily do this by using a BRDF model. Radiance is related to BRDF by the formula

$$L_r(\theta, \phi) = F(\theta_i, \phi_i; \theta, \phi) E_i(\theta_i, \phi_i) \cos \theta_i. \quad (43)$$

where  $L_r$  is the reflected radiance,  $F$  is a BRDF,  $E_i$  is the incident irradiance, and  $\theta_i$  is the angle of the incident radiance [3].

I chose to model four samples with two separate BRDFs for this simulation: a perfectly Lambertian scatterer and three samples using a Cook-Torrance model. A Lambertian scatterer [12] has a BRDF of

$$F(\theta_i, \phi_i; \theta, \phi) = \frac{1}{\pi}. \quad (44)$$

While this model is heavily simplistic, it gives us a good baseline for measuring diffuse samples. A huge number of diffuse samples can be approximated as Lambertian or

Lambertian like scattering patterns.

The Cook-Torrance BRDF model is a significantly more complex model used for simulating specular samples [1].

$$K = \frac{\rho_s}{\pi} \frac{DG}{(\vec{N} \cdot \vec{L})(\vec{N} \cdot \vec{V})} \text{Fresnel}(F_0, \vec{V} \cdot \vec{H}) \quad (45)$$

where  $\vec{N}$  is the normal of the sample,  $\vec{L}$  is the vector of the incident light,  $\vec{V}$  is the vector from the sample to the point being measured (in our case, from the differential area of the detector to the differential area of the sample),  $\vec{H}$  is the half angle vector between  $\vec{V}$  and  $\vec{L}$ ,  $G$  and  $D$  can be found in the equations below,  $\rho_s$  is one of the fitting parameters, and  $\text{Fresnel}()$  calculates the Fresnel reflection of the sample [15]. (For a more complete description of this function and the associated variables, see Cook's paper "A Reflectance Model for Computer Graphics" [16].)

$$G = \min \left\{ 1, \frac{2(\vec{N} \cdot \vec{H})(\vec{N} \cdot \vec{V})}{(\vec{V} \cdot \vec{H})}, \frac{2(\vec{N} \cdot \vec{H})(\vec{N} \cdot \vec{L})}{(\vec{V} \cdot \vec{H})} \right\} \quad (46)$$

$$D = \frac{1}{m^2 \cos^4 \delta} \exp \left( - \left[ \frac{\tan \delta}{m} \right]^2 \right) \quad (47)$$

The  $D$  term contains one of the two fitting parameters of the model, the variable  $m$ .  $\delta$  is the angle between the half angle vector and the normal. "Experimental Analysis of BRDF Models - Supplemental" by Ngan et al. [1] gives examples of this BRDF model with a list of the fitting parameters used. Since the goal is to test the detector and not the sample in this model, several samples were chosen from the paper: a diffuse sample, a specular sample, and one sharing both characteristics.

The *Fresnel* portion of the equation is related to the Fresnel reflection of the

sample [15], and is calculated using the following formula:

$$Fresnel(F_0, \vec{V} \cdot \vec{H}) = \frac{1}{2} \frac{(g - c)^2}{(g + c)^2} \left[ 1 + \frac{[c(g + c) - 1]^2}{[c(g - c) + 1]^2} \right] \quad (48)$$

where

$$c = \cos \theta = \vec{V} \cdot \vec{H} \quad (49)$$

$$g^2 = n^2 + c^2 - 1 \quad (50)$$

$$n = \frac{1 + \sqrt{F_0}}{1 - \sqrt{F_0}}. \quad (51)$$

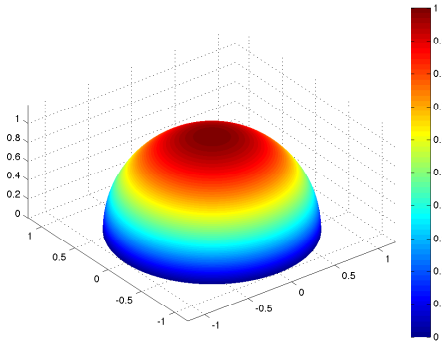
Examining these equations sheds very little light on the operation of the shader, and even less on the operation of the detector, so I will not go into further detail here. What is important is given an index of refraction for the sample, the viewing vector  $\vec{V}$  and the input vector  $\vec{L}$ , the Fresnel reflection of the sample can be calculated.

For this simulation, I used four different BRDF patterns. The first was the perfectly Lambertian case. A Lambertian scatterer provides a good baseline for overall detector efficiency, and is great to study due to the lack of any angle dependence.

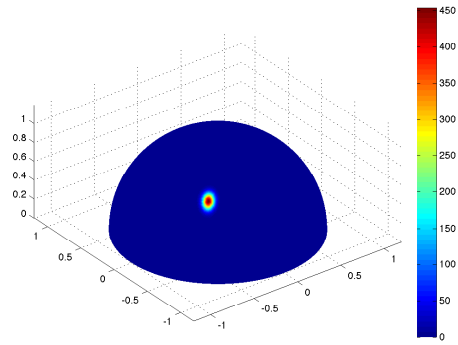
The other three samples were all taken from “Experimental Analysis of BRDF Models - Supplemental” [1]. All three use the Cook-Torrance model detailed above, and have different levels of diffusivity. Their fitting values can be found on Table 3. The sample “acrylic blue” is the most specular of the three, and has a tight specular lobe where most of the energy is concentrated. “black oxidized steel” is a much more diffuse sample, and is a good example of a sample which distributes light unevenly across all five faces of the detector. “ch ball gold metallic 2” is midway between the two, and provides a sample with attributes of each of the previous two simultaneously. The BRDFs of all four scatter patterns can be seen in Figure ??.

**Table 3.** List of sample scatter pattern fitting values. All values were taken from Ngan’s paper ”Experimental Analysis of BRDF Models - Supplemental” [1].

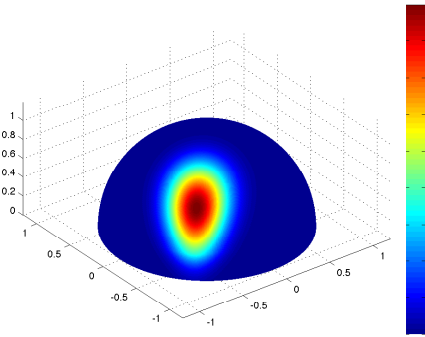
Lambertian:	$F(\theta, \phi) = 1$	
Acrylic Blue:	$F_0 = 0.035$	$m = 0.037$
CH Ball Gold Metallic 2:	$F_0 = 0.629$	$m = 0.144$
Black Oxidized Steel:	$F_0 = 0.035$	$m = 0.19$



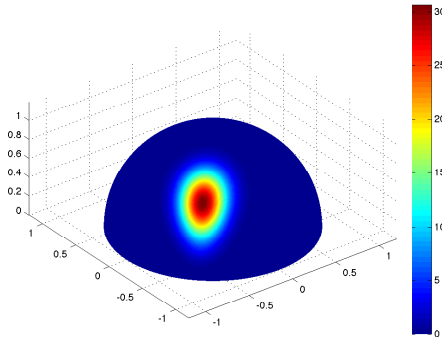
(a) Lambertian Scatterer.



(b) Acrylic Blue Scatterer.



(c) Black Oxidized Steel Scatterer.



(d) Gold Metallic Scatterer.

**Figure 8.** Sample scatter patterns. All figures have units  $\text{sr}^{-1}$ . All patterns were evaluated with  $\theta = 45^\circ$  and  $\phi = 45^\circ$ .

### 4.3 Interpreting Results

Ultimately, the goal of this section is to compare the power measured by the actual detector to that of the ideal detector. The ideal detector power is calculated as a function of angle using the scatter patterns outlined above and doesn't include the absorption term of the detector. This is the actual power reflected by the sample, and the baseline of the comparison. The actual power is the power detected by the detector taking into account the absorption and geometry of the detector. Ideally, these two values should be identical.

Because of the absorption term, the detector must be calibrated to calculate the DHR. This calibration will be further discussed in the section relating to Measurement Theory, V. For now, we are going to implement a single scalar calibration term for calculating the DHR from the power calculated by 42 and 34. These calibration terms are as follows:

$$C_{\text{det}} = \Phi_{\text{det}}(0, 0)^{-1} \quad (52)$$

$$C_{\text{act}} = \Phi_{\text{act}}(0, 0)^{-1}, \quad (53)$$

where the gold metallic sample is used as the scatterer. Basically, this is simply setting the measured DHR of both the simulated detector DHR and the actual DHR equal to 1 at  $\theta = 0^\circ$ . This is equivalent to what is done later on the Measurement Theory section.

### 4.4 Simulation Parameters

In order to simulate the detector, the various values found in Table 2 have to be defined. The values used in this simulation can be found in Table 4. The dimensions of the detector were taken from the actual experiment. The IGAR detector is 10mm

**Table 4. Relevant values for the simulation.**

$x_{\max} = 10$	$\Delta x_d = 0.1$
$y_{\max} = 20$	$\Delta y_d = 0.1$
$z_{\max} = 10$	$\Delta z_d = 0.1$
$x_{s,\max} = 0.5$	$\Delta x_s = 0.1$
$y_{s,\max} = 0.5$	$\Delta y_s = 0.1$

wide by 20mm long by 10mm tall. The range for the sample was chosen such that the specular reflection of the sample was small enough to display the angular dependence of the detector. The  $\Delta$  values were chosen to maintain accuracy while minimizing calculation times. Doubling the  $\Delta$  values drastically increased the time necessary for computations while having negligible effect on the overall calculations.

Note that all of the code used for these calculations can be found below in Appendix B.

## 4.5 Results

The simplest scatter pattern to analyze is the Lambertian case. For this, the actual DHR of the sample (utilizing the calibration terms) is 1.0602. This error shows that the gold scatterer used for calibration does not have a DHR of 1. This kind of error can easily be removed in a real system by accurately measuring the DHR of the calibration mirror. For the detected DHR (the term including the absorption of the detector), the measured DHR has a value of 1.0228. Defining the error as

$$e = \frac{|\Phi_{\text{act}} - \Phi_{\text{det}}|}{\Phi_{\text{act}} + \Phi_{\text{det}}} \quad (54)$$

the error between these two measurements is a little less than 2%.

This result shows two important characteristics of this detector which will be reinforced by the other samples. One, the DHR measurement is not perfect. Even for the

simplest scatterer, there is error associated with this measurement before accounting for other sources of error. This error is caused by the fact that the reflectance, and hence absorptance, of the detector is a function of angle. The light scattered to the edges of the detector are not detected as well as the light scattered to the center of the face.

The second important characteristic is that this result is still very close. Even with poorly calibrated data, the results are still within 2% of each other. Later, it is shown that this error is significantly less than the error caused by the uncertainty of the measurement. For example, the error in measuring the voltage of the detector accounts for uncertainties as great as 4% in the measurement of DHR.

The next scatterer to examine is the Black Oxidized Steel scatterer. This is a very diffuse sample, so results similar to the Lambertian case would be expected. The actual DHR and detected DHR can both be found in Figure 9. Here, we find that both of these values are very close to each other throughout the entire range of  $\theta$  from  $1^\circ$  to  $90^\circ$ . There is still a difference between the two measurements, but it is still very close. The measurement has an average error of 2.5%.

The Acrylic Blue scatter has a much tighter specular lobe than the Black Oxidized Steel scatterer, and because of it has a different error, as seen in Figure 10. The Black Oxidized Steel scatterer error was almost completely positive, indicating that the actual DHR was greater than the detected DHR. The opposite is true for the Acrylic Blue scatterer. Throughout the entire range of angles, the detected DHR was greater than the actual DHR. This scatterer had a smaller error than the previous case, with an average error of 1.7%.

The final scatterer analyzed was the Metallic Gold scatterer. This scatterer had the most unique DHR of the group of samples, as seen in Figure 11. Even with the irregularity of the DHR, the detector was still able to make a very accurate



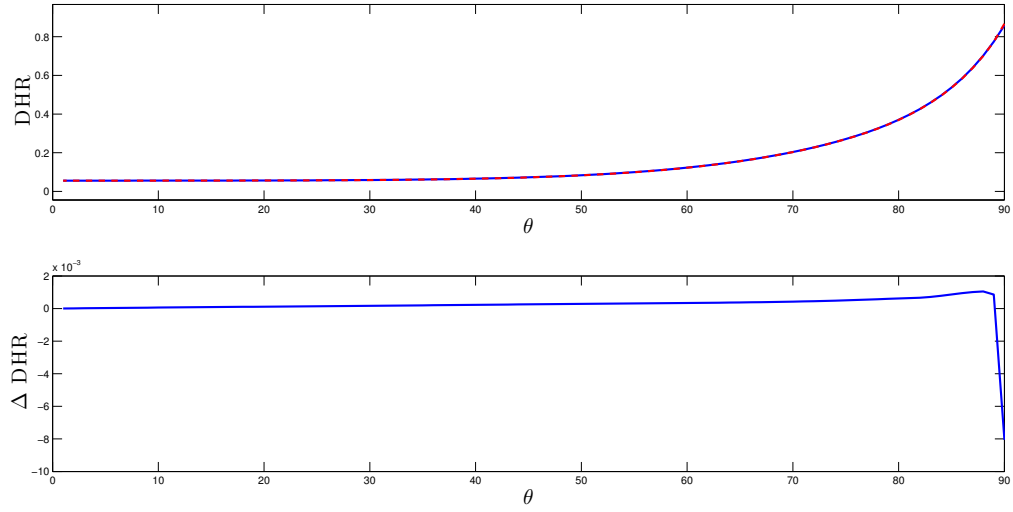


Figure 9. Actual and Detected DHR for the Black Oxidized Steel scatterer. The solid line is the detected DHR, while the dashed line is the actual DHR of the sample.  $\Delta\text{DHR} = \text{Actual DHR} - \text{Detected DHR}$ . The detected DHR varies from less than the actual DHR to greater than the actual DHR, but is still very close.

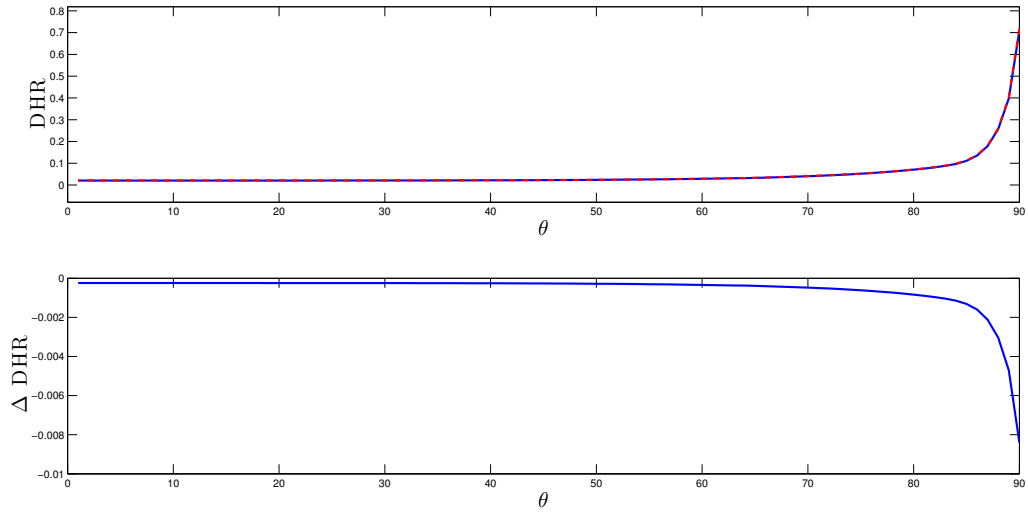
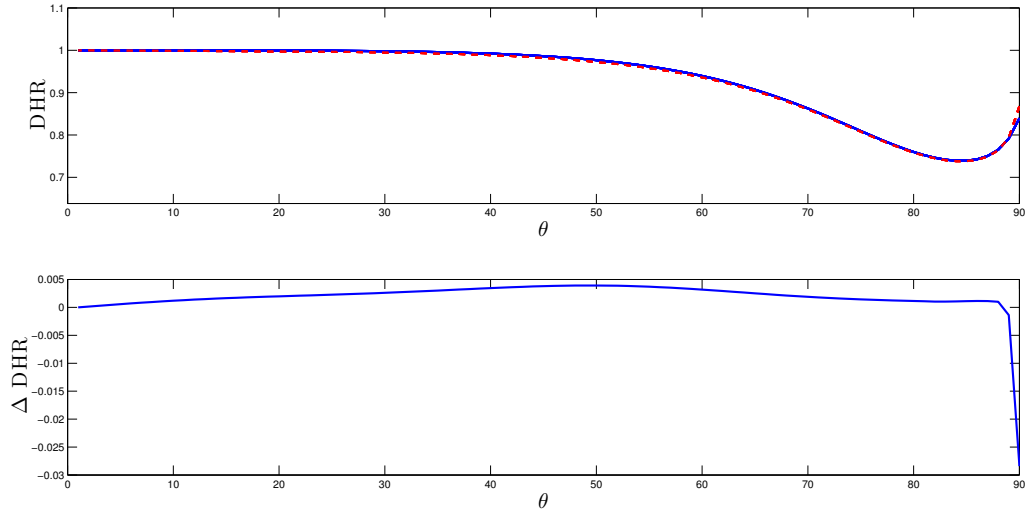


Figure 10. Actual and Detected DHR for the Acrylic Blue scatterer. The solid line is the detected DHR, while the dashed line is the actual DHR of the sample.  $\Delta\text{DHR} = \text{Actual DHR} - \text{Detected DHR}$ . The detected DHR is always slightly less than the actual DHR, but is very close over the entire range of angles.



**Figure 11. Actual and Detected DHR for the Gold Metallic scatterer. The solid line is the detected DHR, while the dashed line is the actual DHR of the sample.  $\Delta \text{DHR} = \text{Actual DHR} - \text{Detected DHR}$ . Even with the complicated nature of this DHR, the Detected and Actual DHR are still very close to each other.**

measurement. The average error of this sample was 2.5%. The most interesting feature of this sample is how much the error varied over the range of angles sampled. The error at  $40^\circ$  is noticeably more than the error at  $10^\circ$ .

## 4.6 Summary

These results demonstrate many important characteristics of the performance of the detector. Firstly, the detector cannot make perfect measurements. Even with the sample which was calibrated to itself, there was a nontrivial error associated with the measurement, before accounting for any uncertainties. However, these errors are low enough that they can be ignored in all situations.

The second result is that the error is a function of angle, and hence cannot be calibrated or corrected out of the system. The detector measured the Blue Acrylic scatterer as having a DHR greater than the actual DHR, while the Black Oxidized

Metal scatterer was measured with a DHR less than the actual DHR. The Gold Metallic scatterer has a DHR significantly different from the other two analyzed scatterers, and hence the most unique error. This error varied significantly as a function of angle. Due to the variety of these errors, they cannot all be calibrated out of the system.

However, in all cases, the measured error was low. The highest measured error over all four samples was 2.55%. In practice, this error is negligible compared to the uncertainty in the measurements taken by the system. Even without being able to absorb all of the light emitted by the sample, the theoretical detector can still make accurate measurements of the power reflected by the sample, and hence the DHR.

## V. Measurement Theory

Given the detector described in , how can DHR be measured in a laboratory setting? As shown in equation (1), two measurements are required: the power reflected by the sample and the power incident on the sample. From Section 3.1, the total power reflected by the sample can be calculated by summing the power seen by the detector, but this glosses over an important aspect of detector operation. The detector does not report power, it reports a voltage. We need to carefully calibrate the detector in order to recover the power. This calibration method is covered in the following sections.

In the sections that follow, it is assumed that the system has access to the following measurements: detector voltage as a function of angle and of face with uncertainties ( $V_{d,j}(\theta)$ ), power seen at the wavemeter with uncertainties ( $P_w$ ), and the reflectivity of the some calibration standard (for this experiment, calibration mirrors were used) with uncertainties ( $\rho_c(\theta)$ ). No other physical parameters of the system need to be known in order to make DHR measurements of the sample.

### 5.1 Basic DHR Measurements

The method that IGAR uses to calculate DHR is derived from equation (1). Knowing the power incident on the sample and the power reflected by the sample, the DHR can be calculated. This can be stated as

$$\rho(\theta) = \frac{\Phi_r(\theta)}{\Phi_i} \quad (55)$$

where  $\rho(\theta)$  is the DHR as a function of angle of incidence,  $\Phi_r$  is the power reflected off the sample, and  $\Phi_i$  is the power incident on the sample. Neither  $\Phi_r$  nor  $\Phi_i$  can be measured directly. Instead, we measure the voltage at the detector and the power at

the wavemeter. We can describe the relationships between these values and  $\Phi_r$  and  $\Phi_i$  as

$$\Phi_r(\theta) = C_d V_d(\theta) \quad (56)$$

$$\Phi_i = C_w P_w \quad (57)$$

where  $C_d$  and  $C_w$  are linear loss and conversion terms,  $V_d$  is the voltage measured at the detector, and  $P_w$  is the power seen by the wavemeter. (Note that  $V_d$  is actually a five element vector, one voltage per face. This will be addressed in Section 5.5.)  $C_d$  and  $C_w$  are coefficients that encompass many linear terms. For example,  $C_w$  includes the losses due to the beamsplitter and power lost due to the input aperture of the wavemeter. While the values of these terms can be calculated explicitly, it is easier to combine these terms and rewrite them in terms of measurable data.

## 5.2 Calculating $C_d$ and $C_w$

Values for both  $C_d$  and  $C_w$  can be calculated explicitly. Both of these constants are related to the optics, efficiencies, and the responsivity of the system.  $C_w$  relates the power seen by the wavemeter to the power output by the laser.

$$C_w = N_{1.0} M_{p1} M_{p2} B \quad (58)$$

where  $N_{1.0}$  is the transmittance of the ND filter,  $M_{p1}$  and  $M_{p2}$  are the reflectivities of the periscope mirrors, and  $B$  is the reflectance of the beamsplitter. Unless the laser power is high enough to cause damage to the optics, all of these values are constants. This means that (57) is always linear.

Calculating the value of  $C_d$  is slightly more difficult, but follows the same pattern.

This value can be expressed as

$$C_d = R_d M_h (1) N_r T_{\lambda/2} T_c (1 - B) \quad (59)$$

where  $R_d$  is the responsivity of the detector,  $M_h$  is the reflectance of the hemi-ellipsoidal mirror,  $N_r$  is the transmittance of the variable ND filter,  $T_{\lambda/2}$  is the transmittance of the half-wave plate,  $T_c$  is the effective transmittance of the chopper, and  $B$  is once again the reflectivity of the beamsplitter.

The only portion of this term that is not explicitly linear is the detector responsivity. The assumption that this value is linear is crucial to the operation of IGAR as it currently functions. If the term is linear, then the techniques detailed in Section 6.4 can be used to calculate a calibration constant, and we can avoid calculating these values entirely. However, if the term is not linear, there is a non-linear term that needs to be accounted for. Some complete description of the voltage-to-power relationship would be required in order to calculate the DHR of the sample. By operating the detector with low incident power, the assumption can be made that the responsivity of the detector is linear.

### 5.3 Atmospheric Effects

One subject that was not addressed in the previous section was the effects of the atmosphere on the system. In the portion of the spectrum covered by this experiment, the atmosphere has a high amount of attenuation, and can have strong local effects [9]. For example, a drop in pressure overnight can lower the attenuation of the atmosphere. Some of these effects can be calibrated out of the system, while others cannot.

The beam train can experience atmospheric effect in three different places: be-

fore the beam splitter, between the beam splitter and the power measurement, and between the beamsplitter and the pyroelectric detector. If the attenuation is constant over time, the drop in power can be calibrated out of the system. The extra attenuation would show up as an extra term in either  $C_w$  or  $C_d$ , or would simply look like a drop in power output from the laser. Recalibrating the system with the atmospheric effects would remedy the problem and remove this source of error from the measurement.

Attenuation as a function of time cannot be so easily be corrected. If the attenuation occurs before the beam splitter, the system can still make an accurate measurement. The system will observe a drop in power, but the ratio between the wavemeter and the pyroelectric detector will remain unchanged. If the attenuation occurs after the beam splitter, one of the detectors will see less power than the other, and the ratio between the two will differ.

In practice, these problems have not been observed. Data collected from the same sample with different calibrations remained accurate despite possible changes in the atmosphere. Overall, the lack of change in our measurement proves the robustness of our calibration methodology.

Other DHR systems, such as the SOC-100, circumvent this problem by forcing their reference beam to follow nearly the same path as their beam interrogating the sample. Because both beams have very similar paths, they are both attenuated by the same amount. The sample beam is normalized by the reference beam, and any attenuation due to atmospheric effects is canceled out.

## 5.4 Calibration

Using equation (56), the value of the calibration coefficient can be expressed as

$$C_d = \frac{\Phi_{rc}(\theta_c)}{V_{dc}(\theta_c)}. \quad (60)$$

where the  $c$  subscript implies a value measured during calibration. Using equation (55), this equation becomes

$$C_d = \frac{\rho_c(\theta_c)\Phi_{ic}}{V_{dc}(\theta_c)}. \quad (61)$$

equation (57) allows this term to be rewrite in terms of measurable data and a single unknown:

$$C_d = C_w \frac{\rho_c(\theta_c)P_{wc}}{V_{dc}(\theta_c)}. \quad (62)$$

This implies that the value of  $C_d$  can be calculated in terms of  $C_w$  if the calibration DHR, the power at the wavemeter during calibration, and the voltage at the detector are known during the calibration.

Further simplifications will allow the  $C_w$  term to be removed from the equation entirely. Substituting (62) into (56),

$$\Phi_r(\theta) = C_w \rho_c(\theta_c) \frac{P_{wc}}{V_{dc}(\theta_c)} V_d(\theta). \quad (63)$$

Substituting both this and (57) into (55),

$$\rho(\theta) = \frac{C_w \rho_c(\theta_c)}{C_w P_w} \frac{P_{wc}}{V_{dc}(\theta_c)} V_d(\theta) \quad (64)$$

which simplifies to

$$\rho(\theta) = \frac{\rho_c(\theta_c)P_{wc}}{V_{dc}(\theta_c)} \frac{V_d(\theta)}{P_w}. \quad (65)$$



Combining the calibration terms into a single variable, the DHR can be calculated as

$$\rho(\theta) = C_c \frac{V_d(\theta)}{P_w} \quad (66)$$

where

$$C_c = \rho_c(\theta_c) \frac{P_{wc}}{V_{dc}(\theta_c)}. \quad (67)$$

What this means is that IGAR can be calibrated only using data measured by the system. No information regarding any of the optics, lasers, or detectors need to be known in order to make DHR measurements. This affords much flexibility for the system. The laser or the optics of the system can be changed without making any changes to the operation of the system.

## 5.5 Making Measurements

Equation (66) ignores one significant aspect of IGAR. There is not a single detector; there are five. However, as shown in (21), the total power reflected by the sample is equal to the sum of the power detected by each face of the detector. Unfortunately, these powers are not known. The only data recorded by the system is the voltage of each face of the detector.

Starting again at equation (56), a single DHR value can be calculated in the following manner. In this equation,  $\Phi_r$  is the power seen by the entire detector. The power seen by the entire detector is simply the sum of all the power seen by all the faces. This can be written as

$$\Phi_r(\theta) = \sum_{j=1}^5 \Phi_{r,j}(\theta) = \sum_{j=1}^5 C_{d,j} V_{d,j}(\theta_j). \quad (68)$$

In this equation,  $\Phi_{r,j}$  is the power seen by face  $j$ ,  $C_{d,j}$  is the calibration coefficient of

face  $j$ , and  $V_{d,j}$  is the voltage seen on face  $j$ .

In order to make this measurement, we need to calculate  $C_{d,j}$ . This can be done exactly the same way it was done before. Equation (62) can be rewritten as a function of face:

$$C_{d,j} = C_w \frac{\rho_c(\theta_{c,j}) P_{wc,j}}{V_{dc,j}(\theta_{c,j})}. \quad (69)$$

It is important to note that  $C_w$  is not a function of face, as it is derived from the optics relating to the wavemeter.

Combining (68), (69), and (57) into (55),

$$\rho(\theta) = \frac{1}{C_w P_w} \sum_{j=1}^5 C_w \frac{\rho_{c,j}(\theta_{c,j}) P_{wc,j}}{V_{dc,j}(\theta_{c,j})} V_{d,j}(\theta). \quad (70)$$

The  $C_w$  terms cancel, and all the calibration terms can be again combined into a single constant as a function of face. This makes the equation for calculating DHR

$$\rho(\theta) = \sum_{j=1}^5 C_{c,j} \frac{V_{d,j}(\theta)}{P_{w,j}} \quad (71)$$

where

$$C_{c,j} = \rho_{c,j}(\theta_{c,j}) \frac{P_{wc,j}}{V_{dc,j}(\theta_{c,j})}. \quad (72)$$

It is important to note that writing the calibration constant in this way gives complete control over how the machine is calibrated. The DHR of the calibration sample and the angle of incidence can both be chosen as a function of face. This means samples and angles can be chosen such that the voltage on the face are maximized during calibration, giving more accurate calibrations.

## 5.6 Uncertainty

In any measurement, there is some uncertainty. In this particular measurement, there are five different sources of error: voltage measured during the measurement, power measured during the measurement, voltage measured during calibration, power measured during calibration, and the DHR of the calibration mirror. In order to better understand these uncertainties and their effect on the measurement of the DHR, begin by assuming that the system is perfectly calibrated. Beginning with equation (71),

$$\rho(\theta) + \Delta\rho(\theta) = \sum_{j=1}^5 C_{c,j} \frac{V_{d,j}(\theta) + \Delta V_{d,j}(\theta)}{P_w + \Delta P_w} \quad (73)$$

which expands to

$$\rho(\theta) + \Delta\rho(\theta) = \sum_{j=1}^5 C_{c,j} \frac{V_{d,j}(\theta)}{P_w} + \sum_{j=1}^5 \frac{C_{c,j}}{P_w} \left[ \frac{V_{d,j}(\theta)}{P_w} \Delta P_w + \Delta V_{d,j}(\theta) \right] \quad (74)$$

which simplifies to

$$\rho(\theta) + \Delta\rho(\theta) = \rho(\theta) + \rho(\theta) \frac{\Delta P_w}{P_w} + \sum_{j=1}^5 \frac{1}{P_w} C_{c,j} \Delta V_{d,j}(\theta). \quad (75)$$

Therefore, the error in DHR for the system, assuming a perfect calibration, is

$$\Delta\rho(\theta) = \rho(\theta) \frac{\Delta P_w}{P_w} + \sum_{j=1}^5 C_{c,j} \frac{\Delta V_{d,j}(\theta)}{P_w}. \quad (76)$$

A more complete derivation of this equation can be found in Appendix A.

Calculating the error for the calibration coefficient is slightly more difficult. In (72), we have three variables with uncertainties. Acknowledging uncertainties, this

equation becomes

$$C_c + \Delta C_c = (\rho_c(\theta_c) + \Delta\rho_c(\theta_c)) \frac{P_{wc} + \Delta P_{wc}}{V_{dc}(\theta_c) + \Delta V_{dc}(\theta_c)}. \quad (77)$$

The  $j$  designator on  $C_c$ ,  $\rho_c$ , and  $V_{dc}$  have been omitted for clarity. Expanding the division term, this equation becomes

$$C_c + \Delta C_c = (\rho_c(\theta_c) + \Delta\rho_c(\theta_c)) \left[ \frac{P_{wc}}{V_{dc}(\theta_c)} + \left[ \frac{P_{wc}}{V_{dc}(\theta_c)} \frac{\Delta V_{dc}(\theta_c)}{V_{dc}(\theta_c)} + \frac{\Delta P_{wc}}{V_{dc}(\theta_c)} \right] \right]. \quad (78)$$

Next, we need to multiply out the  $\rho + \Delta\rho$  term:

$$C_c + \Delta C_c = \rho_c(\theta_c) \left[ \frac{P_{wc}}{V_{dc}(\theta_c)} + \left[ \frac{P_{wc}}{V_{dc}(\theta_c)} \frac{\Delta V_{dc}(\theta_c)}{V_{dc}(\theta_c)} + \frac{\Delta P_{wc}}{V_{dc}(\theta_c)} \right] \right] + \Delta\rho_c(\theta_c) \frac{P_{wc}}{V_{dc}(\theta_c)}. \quad (79)$$

Simplifying,

$$C_c + \Delta C_c = C_c + \left[ C_c \frac{\Delta V_{dc}(\theta_c)}{V_{dc}(\theta_c)} + \rho_c(\theta_c) \frac{\Delta P_{wc}}{V_{dc}(\theta_c)} \right] + \Delta\rho_c(\theta_c) \frac{P_{wc}}{V_{dc}(\theta_c)} \quad (80)$$

or

$$\Delta C_c = \frac{1}{V_{dc}(\theta_c)} [C_c \Delta V_{dc}(\theta_c) + \rho_c(\theta_c) \Delta P_{wc} + P_{wc} \Delta\rho_c(\theta_c)]. \quad (81)$$

Now, the effects of uncertainty in calibration on the measurement can be examined. Going back to equation (76),

$$\Delta\rho(\theta) = \rho(\theta) \frac{\Delta P_w}{P_w} + \sum_{j=1}^5 \left[ (C_{c,j} + \Delta C_{c,j}) \frac{\Delta V_{d,j}(\theta)}{P_w} \right]. \quad (82)$$

From (81),  $\Delta C_{c,j}$  is seen to be a term composed only of other  $\Delta$  terms. This allows

the equation to be simplified to

$$\Delta\rho(\theta) = \rho(\theta)\frac{\Delta P_w}{P_w} + \sum_{j=1}^5 C_{c,j}\frac{\Delta V_{d,j}(\theta)}{P_w}. \quad (83)$$

Interestingly, the uncertainty in the calibration has no effect on the uncertainty of the measurement for small uncertainties. (For more significant uncertainties, the  $\Delta C_{c,j}\Delta V_{d,j}$  cross term cannot be ignored. In practice, this case does not occur.)

All of the above equations are only true if the uncertainties are much smaller than their measurements. For  $P_w$ ,  $P_{wc}$ ,  $\rho_c$ , and  $V_{dc}$ , this is always true. The laser is always strong enough to give the wavemeter a good measurement, the calibration sample is a mirror with around 97% reflectivity, and the detector's voltage during calibration is typically fairly high. However, this assumption is not always true to the voltage on the detector face during sample measurements. Samples with low DHR's have low voltages with significant uncertainties.

## 5.7 IGAR Algorithm

Due to the uncertainties in the measurement, simply summing the powers of all of the faces together increases the uncertainty of the DHR measurement. For the case of a diffuse sample, all faces give the system information about the sample, as all five faces can see light reflected by the sample. This is not the case for all samples. For example, a specular sample might illuminate only a single face. In this case, one of the faces is contributing information about the DHR of the sample, and the other four are contributing noise.

To combat this, NGC implemented an algorithm to minimize this uncertainty [6]. This algorithm is described later in Section 7.2. In a mathematical sense, it functions

as a sifting feature inside the summation of equation (71).

$$\rho(\theta) = \sum_{j=1}^5 C_{c,j} \frac{V_{d,j}(\theta)}{P_w} I_j \quad (84)$$

The addition of this function inside the summation makes equation (83) into

$$\Delta\rho(\theta) = \rho(\theta) \frac{\Delta P_w}{P_w} + \sum_{j=1}^5 C_{c,j} \frac{\Delta V_{d,j}(\theta)}{P_w} I_j. \quad (85)$$

If the face in question has no light incident on it, the voltage will be close to zero. This means that in equation (84), it will be contributing almost nothing to the DHR. Therefore, the inclusion of the  $I_j$  term will have no effect on the measured DHR. However, it makes a significant difference in equation (85). Even with no power incident on a face, the system can still measure uncertainty for that face's voltage. The  $I_j$  term effectively nullifies that portion of the uncertainty, meaning that the overall uncertainty of the measurement is decreased. This leads to overall more accurate DHR measurements by intelligently selecting which faces are measured for any particular sample.

## 5.8 Summary

By carefully defining how IGAR makes measurements, calibration can be performed without any previous knowledge of the optics of the system. This allows maximum flexibility in making measurements. The laser source and optics can easily be adjusted for making any measurement without sacrificing measurement accuracy. This measurement theory was implemented at AFIT and used to measure the DHR of a number of samples.

## VI. Equipment Description

So far, only the theory of the IGAR system has been discussed. Actually implementing these theories in equipment is a challenging task. The next few sections will examine some of the pieces of equipment used to realize the above equations, and address the problems and solutions related to implementing the theories presented in this paper.

### 6.1 Theory of Operation

The goal of IGAR is simple. We want to calculate the DHR of a sample using equation (84). Looking back at that equation, there are only two pieces of information which are required: the power incident on the sample and the power reflected off the sample. This can be accomplished using two detectors. A Bristol Wavemeter measures laser power using the detector used in measuring the wavelength. A novel five sided pyroelectric detector is used in conjunction with a hemiellipsoidal mirror to calculate the power of the light reflected off the sample. Additional information is collected to calculate the uncertainty of the measurement, so that the equipment can ultimately say this is the DHR of the sample at this wavelength and angle with this amount of uncertainty.

### 6.2 Hardware

IGAR can be decomposed into three main pieces: the tunable laser, the hemi-ellipsoidal mirror, and the detector, arranged in the manner shown in Figure 12. A photo of IGAR can be found in Figure 13. Light is emitted by the laser, and directly illuminates the sample mounted at the lower focal point of the hemi-ellipsoidal mirror, as depicted in Figure 12. A portion of the beam is diverted away for measurements

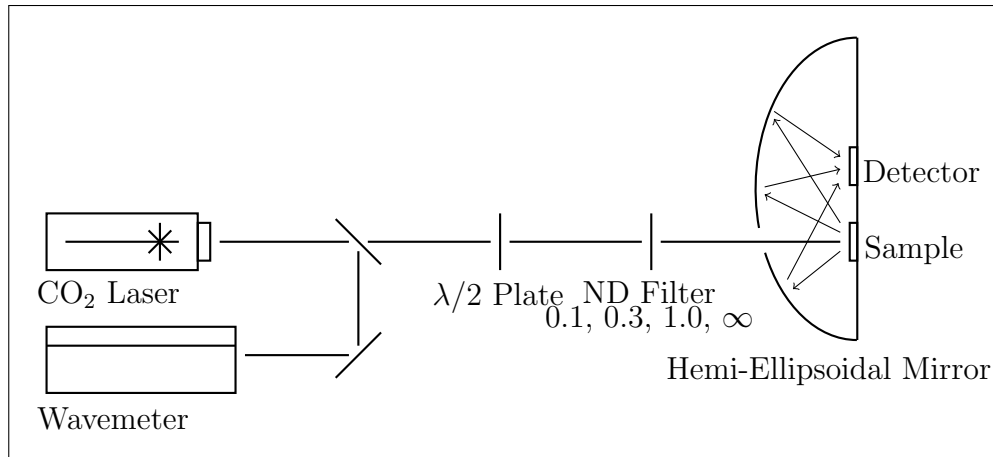


**Figure 12. Functional diagram of the IGAR system.**

performed by the Bristol 741 Wavemeter, manufactured by Bristol Instruments of Victor, NY. Both the mirror and the sample are mounted to a rotation stage, allowing control of the angle of incidence of the laser light. The light is reflected off the sample and onto the mirror. The mirror then focuses the light to the second focal point, where the pyroelectric detector is mounted. This signal is measured by the software, which then calculates the DHR value.

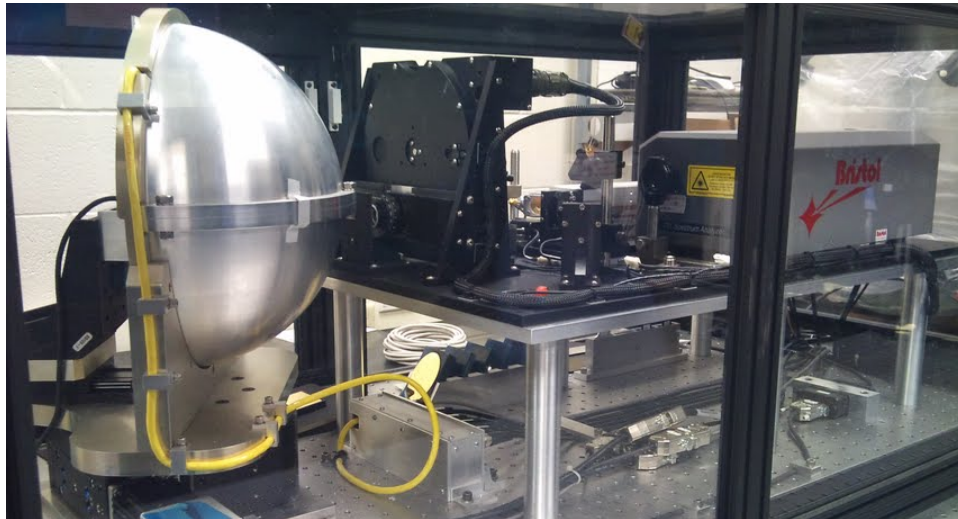


**Figure 13. Photograph of the IGAR system.**

Northrop Grumman chose a LASY-4G tunable CO<sub>2</sub> laser, manufactured by Access



Laser of Everett, WA, as the illumination source for IGAR [5]. This laser has ten useable laser lines ranging from  $9.271\mu\text{m}$  to  $10.718\mu\text{m}$ , and was an excellent choice for several reasons. First, the laser's tunability allows the equipment to cover a good portion of the LWIR atmospheric window, a part of the spectrum of particular interest to the Air Force. Second, the spacing of the laser lines allows for a good spectral coverage, while the spacing between them ensures that the equipment will not accidentally tune to the wrong wavelength. The low power of the laser allows enough light to illuminate the sample while never damaging the material. (The spec sheet lists the maximum power as 400mW, while in-house measurement places this value closer to 40mW. Individual lines can be even weaker.) Northrop Grumman did extensive testing regarding the stability and structure of each wavelength's modes, ultimately deciding on ten wavelengths with the best structure. The laser can easily be run continuously, and the software allows for laser tuning automatically. All of this means that the sample can be placed in the instrument, and reliably measured without operator intervention.

Several months after receiving IGAR, the LASY-4G laser malfunctioned. As a temporary measure, the laser was replaced with one of Daylight Solutions' external cavity quantum cascade lasers (QCL). This laser shifts the portion of the spectrum which we are using from the LWIR portion of the spectrum to the MWIR. The laser currently being used operates from  $5.2$  to  $5.9\mu\text{m}$ , and can easily be replaced by any of the other QCLs in AFIT's possession [17]. This allows the range of useable wavelengths to be extended to  $4.84 - 9.7\mu\text{m}$ . Furthermore, this demonstrates that the lasers are easily interchangeable. The only attribute that limits this range is the responsivity of the pyroelectric detector. While this specific pyroelectric detector has not been extensively tested, most detectors have a wide range of useable wavelengths, covering the majority of the infrared portion of the spectrum.

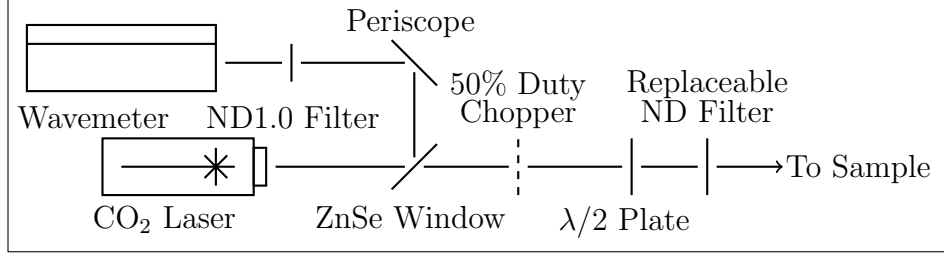


**Figure 14. Diagram of optics used in IGAR.**

Due to the tunable nature of the instrument, some way to accurately and reliably measure the wavelength of the laser was needed. For this, a Bristol 721 wavemeter [11] was used. The wavemeter reports both power and wavelength back to the software. Both of these values are used for the tuning of the CO<sub>2</sub> laser. The tuning of the QCLs happen external to the program. Wavelengths are recorded during every sample to ensure that the laser was stable over the entire measurement, and the power measurement is used directly by the software to calculate the DHR of the sample, as detailed in Section 6.1.

Laser light is passed through a series of optics before illuminating the sample, as shown in Figure 14. This diagram is accurate while using the CO<sub>2</sub> laser. Using a QCL requires an additional two mirrors before the beamsplitter for alignment. A zinc selenide beam splitter picks off part of the beam for spectral measurements. A 50% duty cycle chopper is used in conjunction with a lock-in amplifier to reduce measurement noise. A half-wave plate was included to control the orientation of the polarization. A replaceable ND filter (0.1, 0.3, or 1.0) can be placed to reduce beam signal if necessary. A beam blocker can also be placed in front of the beam for background measurements if necessary. After the filter, the light illuminates the sample. This light is reflected and focused by the mirror.

Northrop Grumman had Aero Research Associates Inc. of Holbrook, NY, make the hemi-ellipsoid mirror for IGAR [7]. This mirror has a major axis of 10.77" and a minor axis of 10.583". This leads to a spacing of 2" between the upper and lower

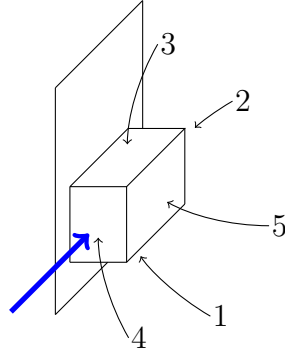


**Figure 15. Diagram of the detector. The thick arrow is laser light's vector reflected from the sample off the mirror at a high angle of incidence.**

foci, where the detector and sample are mounted respectively. A slot 0.40" wide in the front of the mirror allows the laser light into the hemisphere to illuminate the sample. Because the sample is mounted at one focal point of the mirror, all of the light reflected by the sample is reflected off the mirror to the second focal point, where the detector is mounted. The mirror has  $> 96\%$  reflectance throughout the IR, as measured by NGC [6], ensuring that nearly all of the reflected light is collected and delivered to the detector.

Finally, the light is collected by the detector. Northrop Grumman designed a five-sided pyroelectric detector for the sensor of this system. The detector can be seen in Figure 15. The power incident on each face is measured independently and reported to the software. An external controller is used with the detector, and allows the software to specify a time constant for the measurement. Northrop Grumman claims that there is some noise inherent to the system due to crosstalk between the detector channels; we at AFIT have not seen this become an issue during measurements. This effect is particularly apparent with specular samples when the signal shifts between faces. Northrop has plans to enhance the detector by allowing each face to be powered and measured separately, eliminating this problem.

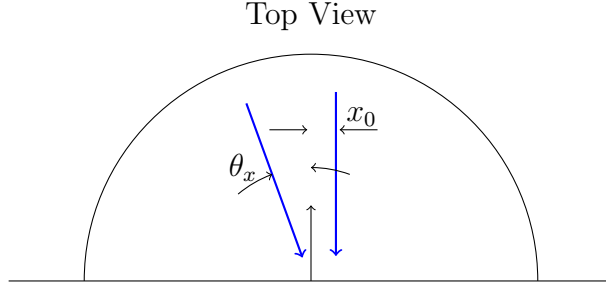


**Figure 16.** *x* angular and positional misalignment.

### 6.3 Alignment

As with any optical system, it is crucial to have good alignment. IGAR is no exception. By using the small angle approximation, any misalignment in the system can be described as a combination of four independent misalignments, each with their own unique characteristics. These four misalignments are *x* angular, *x* positional, *y* angular, and *y* positional. A diagram of these four cases can be seen below in Figures 16, 17, and 18. Some of these will adversely effect the performance of the system, while others can be ignored entirely.

*x* angular misalignment is when the beam is oriented at some angle away from the sample plane's normal, but still parallel to the plane of the optical bench. This misalignment will still allow the equipment to capture uncorrupted measurements from the system, but there will be an angular offset present in the data. Due to the novel nature of this instrument, it is difficult to use the data collected by other instruments to identify this misalignment. In order to identify this misalignment, a sample with a distinctive, angle dependent DHR would be needed. For instance, a sample with a peak at a known angle. Without this sort of sample, this misalignment cannot be identified. However, the small angle approximation made earlier makes this misalignment negligible.

The second angular misalignment is the *y* angular misalignment, as shown in Figure 17. This misalignment is negligible for small angles. For instance, consider

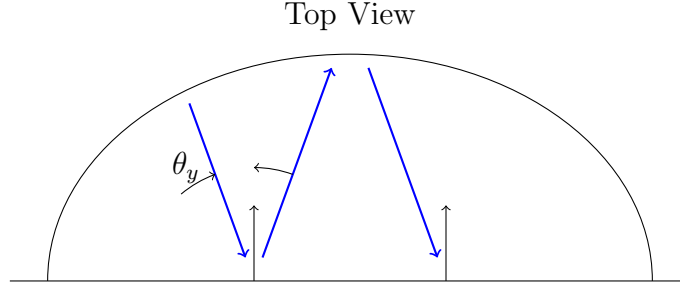


**Figure 17.  $y$  angular misalignment.**

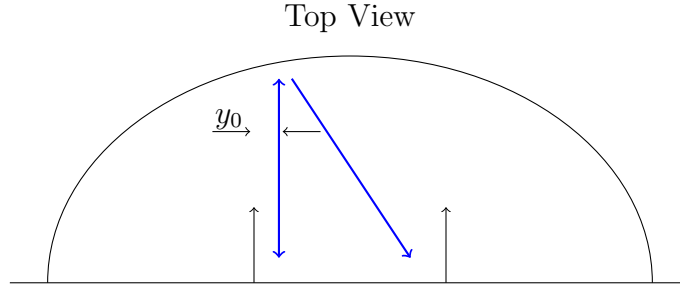


**Figure 18.  $y$  positional misalignment.**

the case where there is a flat mirror in the sample slot. The beam misalignment will simply move the spot on the hemiellipsoidal mirror slightly up or down. Due to the shape of the mirror, this beam will still travel through the second foci. For small angles, this misalignment has no effect on measurements.

The other two possible misalignments are  $x$  and  $y$  positional, as seen in Figures 16 and 18 respectively. Both of these are best understood by, again, examining the detector in image space, which is the sample plane. The mirror does introduce some aberrations in the system, which can be ignored thanks to the small angle approximation. Positional  $y$  misalignment is the easiest to analyze. Assuming again that there is only a small misalignment, the system will be only slightly impacted. The beam spot on the detector simply moves up the face of the detector.

$x$  positional misalignment is the most difficult to analyze due to the geometry of the problem. In all of the other misalignments, the rotation of the sample plane throughout the measurement can be ignored. Here, this effect cannot be ignored;

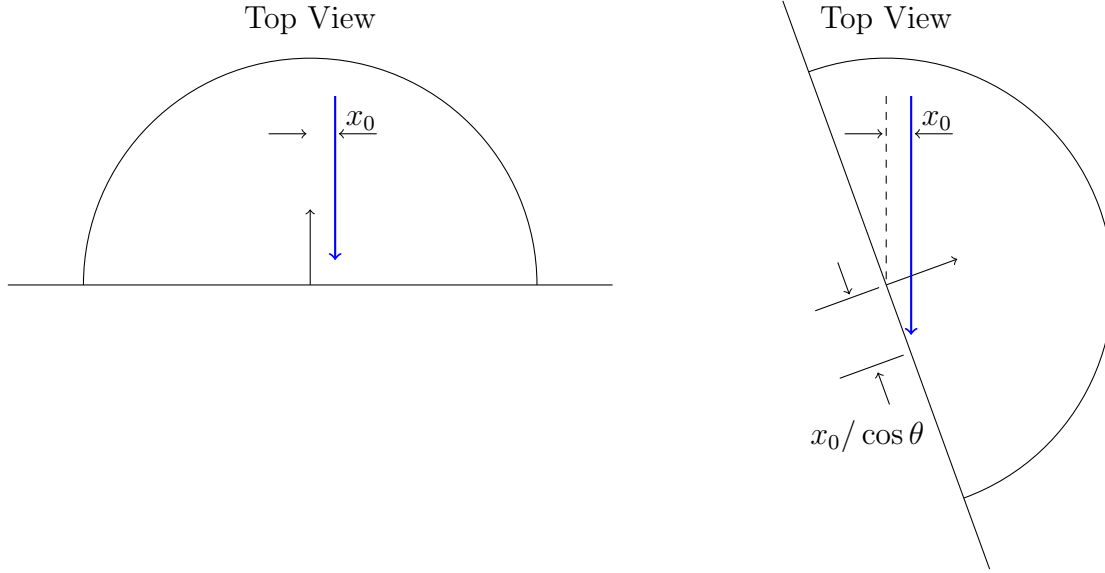


**Figure 19.**  $x$  positional misalignment at normal incidence and at  $70^\circ$ .

rotating the sample plane means that the  $x$  positional misalignment grows. If  $x_0$  is the distance from the sample center to the beam center at normal incidence, the distance at some angle  $\theta$  is  $x_0 / \cos(\theta)$ . IGAR begins to make measurements at  $30^\circ$ , meaning that this length is already 15% larger when you begin the measurement. At the highest angle, this distance has grown to 11 times the original distance. This error at both normal incidence and high angles of incidence can be seen below in Figure 19.

If we are analyzing the system with rays, this offset is mostly insignificant. As long as the ray still hits the detector, theoretically we can still measure the power. With a detector size of about 20mm, we can be off by as much as 1mm and still make measurements. However, this analysis ignores the width of the beam. If the beam is 2.5mm wide, at 85 degrees, the power of the beam is distributed over 28mm. Even with no misalignment, over 20% of the power is cast in such a way that it cannot be seen by the detector. With a misalignment as little as 1mm at normal incidence, the power lost increases to 35%. This amount of misalignment can drastically impact the accuracy of measurements made at high angles of incidence.

An easier method for proper alignment might have been including an alignment mirror. This mirror would be oriented at 45degrees from normal in the same holders as the calibration mirrors. A retroreflection would allow the user to make sure that the laser is properly aligned to the sample plane, allowing much greater confidence in the quality of the measurement.

## 6.4 Calibration

As shown above in section 6.4, IGAR can be calibrated using the equation

$$C_{c,j} = \rho_c(\theta_{c,j}) \frac{P_{wc,j}}{V_{dc,j}(\theta_{c,j})}. \quad (86)$$

In this equation,  $\rho_c(\theta_c)$ ,  $P_{wc,j}$  and  $V_{dc,j}(\theta_{c,j})$  are all known or measurable quantities. This allows the equipment to easily calculate the value of the calibration coefficient. Actually making these measurements is a bit more difficult.

The first term,  $\rho_{c,j}(\theta_{c,j})$ , is the easiest to find. All that is needed is the reflectivity of whatever sample we use to calibrate the system. In practice, a gold coated mirror is used for calibration. This mirror has high reflectivity over the entire IR portion of the spectrum, about 97%. It is important to note that the angle of incidence is included in this term. This has less to do with the reflectivity changing as a function of angle as it does with the orientation of the mirror during calibration. The angular dependence of this sample can be calculated using Frensel's equations. For other samples, a measurement of the angular characteristics of the calibration sample would need to be known.

The next term is  $P_{wc,j}$ . This is simply a measurement of the incident power during the calibration. The wavemeter can easily make this measurement and relate it to the system for calculations. The incident power is measured as a function of face to

allow for the power of the laser to drift even during calibration. This allows an even more robust system with no cost to either complexity or measurement time.

Finally, there is the term  $V_{dc,j}(\theta_{c,j})$ . There are three important aspects of this measurement: the voltage, the angle of incidence and the face being measured. This calibration method allows each face to be calibrated individually, but comes with the cost that all of the reflected power is incident onto a single face. Without this being true, the reflectivity that the detector sees would be distributed between multiple faces, meaning that the  $\rho_c$  term is not actually known. By controlling the orientation of the sample, the system can be adjusted such that all of the light incident on the calibration sample will be reflected to the face of the detector being calibrated.

When this assumption holds true, the power incident on the calibration mirror, the reflectivity of the mirror, and the voltage of the detector for the incident power are all known quantities. With these measurements, the system can be calibrated, and used for making DHR measurements.

Originally, Northrop Grumman designed IGAR to be calibrated before and after making a set of measurements. This was due to the fact that initially, IGAR had no way to measure the power of the laser during the measurement. Originally, IGAR was designed to omit the  $P_w$  and  $P_{wc}$  terms from the DHR equation and calibration equation. Instead, the power was measured before the initial calibration and after the final calibration. If these two numbers were the same, the power could simply be ignored.  $P_w = P_{wc}$ , and could be eliminated from the equation. If these two numbers were close, a linear gradient was applied to the data. This effectively functioned as a  $P_w$  that increased from the initial value to the final value over the course of the measurement. By adding the wavemeter to the system, the incident power could be measured in real time, which eliminated the need for this scaling effect, and allowed the final calibration to be ignored.



Eventually, further testing revealed the initial calibration could be forgone as well. Calculating the calibration coefficient as done in Equation (86) gave the system the flexibility needed to do this. By including the power term, any short or long term variations in the laser power could be accounted for. The responsivity of the detector does not change (except as a function of wavelength), which makes this term more or less a constant. Now, calibration is only performed as a verification method, or when the wavelength of the laser is changed.

Note that there is some small wavelength dependence in the responsivity of the detector. A pyroelectric detector functions on the change in temperature of the material covering the detector, making the detector responsivity a function of the absorptance of the material used to cover the detector. In practice, the material covering the detector is a dark, very absorptive material, making this dependence on wavelength negligible. Even without this assumption, this responsivity term is absorbed into the calibration coefficient, and can be calibrated out of the measurement.

At one point, Northrop Grumman considered using a diffuse sample to calibrate all five detector faces simultaneously. The idea was that a diffuse sample would illuminate each face identically. Knowing the incident power, and that this incident power was equally distributed between all five faces, the calibration constants could be calculated simultaneously. In theory, this could work: knowing the reflectivity of a diffuse sample and the size of the faces, the incident power could easily be calculated. However, there are no well defined diffuse DHRs in the LWIR portion of the spectrum. At shorter wavelengths, a sample like Spectralon or Infragold would function well. However, there are no diffuse NIST traceable standards around the  $10\mu\text{m}$  wavelength that could be used to calibrate the machine. Northrop instead opted for the multiple mirror calibration methodology previously described.

## 6.5 Software

All of the software for IGAR was written in Labview. The majority of the code is used to facilitate the use of the device, controlling parameters such as angle of incidence and operating the pyroelectric detector. However, there are a few sections of the code which are worth discussing here. One of these is the laser autotuning subroutine. This subroutine is used for automatically tuning the CO<sub>2</sub> laser to the desired wavelength and optimizing the power. Creating an algorithm to do this turned out to be nontrivial due to nonlinearities in the laser. For instance, the optimal position of the micrometer used for tuning the laser would shift depending on the temperature of the laser housing. Another significant portion of the code is used to calculate the power incident on the pyroelectric detector. This algorithm analyzes the data on all five faces to determine which ones will yield the most accurate measurement.

## VII. Algorithms

There are two notable algorithms implemented in this software that are used by IGAR to enable and aid measurements. The first of these is the Laser Autotuning algorithm. This algorithm is an automated sequence which is used by the software to control the CO<sub>2</sub> laser previously mentioned. This method allows the equipment to tune the laser to the desired wavelength without operator intervention, allowing the system to make DHR measurements of a single sample at multiple wavelengths efficiently. The second is the algorithm mentioned in Section 5.7. This algorithm intelligently selects which faces are used to calculate the DHR in order to reduce the uncertainty of the measurement. Both of these algorithms were written in Labview and have been extensively tested in laboratory work.

### 7.1 Laser Autotuning Algorithm

The laser auto tuning subroutine was designed to automatically tune the CO<sub>2</sub> laser to the desired wavelength without operator intervention. The CO<sub>2</sub> laser is a grating-tuned laser with a computer controlled micrometer moving the grating. Tuning the laser to the desired wavelength proved to be nontrivial. The peak power and exact position of the micrometer for a single wavelength tended to shift depending on external conditions. The exact position varied, but by a small enough amount that the approximate position of the wavelength is known.

Knowing this approximate position, I designed an algorithm to tune the laser to the peak power at the desired wavelength. The diagram of this process can be seen in 20. The subroutine functions as follows. First, the micrometer is moved just short of the approximate position of the peak power. The micrometer is then incremented forward until lasing is observed. At this point, the wavelength is checked by the

wavemeter. Assuming the wavelength is the one we are looking for, the subroutine continues moving the micrometer forward until the power of the laser begins to drop. At this point, the micrometer backs up, and begins moving forward again with smaller steps. This process is repeated three times. Once the peak is identified, the micrometer resets, and moves to the recently measured peak position. The wavelength is checked once again and recorded. The entire process takes about five minutes, and has been extensively tested. It will reliably find the peak power with no operator intervention, allowing us to run a single sample at multiple wavelengths.

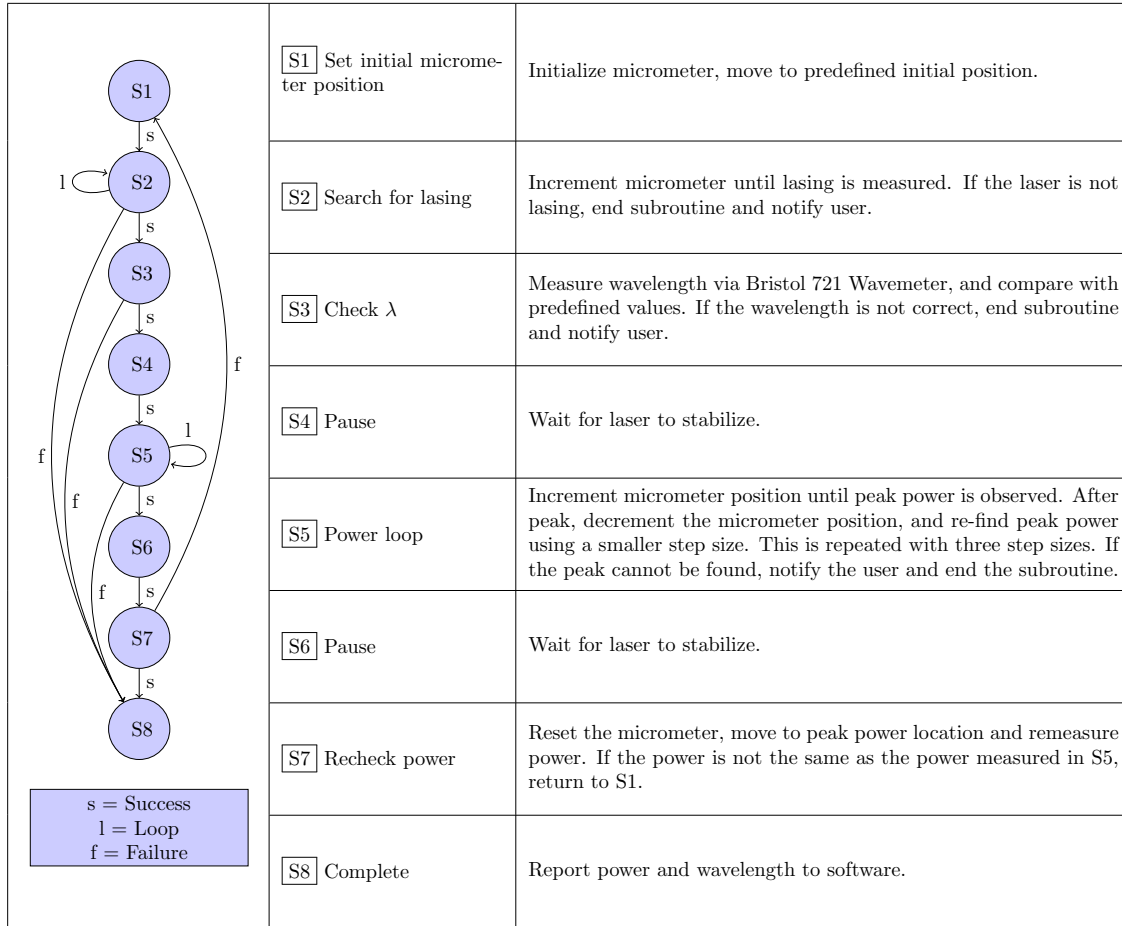


**Figure 20. Algorithm for automatically tuning the CO<sub>2</sub> laser to the desired wavelength without operator intervention.**

## 7.2 IGAR Algorithm

The other notable piece of code is the algorithm for calculating the power reflected off the sample using the measurements from the pyroelectric detector. To capture the data, the software takes measurements at a variety of time constants with a variable number of measurements. The mean voltage and standard deviation are calculated, which are converted into power measurements using the calibration data, as detailed in Chapter V. The algorithm is then called to calculate the most accurate power measurement using the data from all five faces.

The algorithm, designed by Northrop Grumman, works based on the assumption that not all faces are contributing data to the measurement. For instance, if all of the power is incident only on one face, four of the faces are contributing nothing but noise to the measurement. By carefully ignoring these noncontributing faces, the measurements can be made more accurate. The algorithm operates in this manner, and can be seen in Figure 21.

To begin, the algorithm calculates the power and uncertainty using all five faces. Both of these are simply the sums of their respective parts. Next, the algorithm drops the face with the lowest power from set. Power and uncertainty are recalculated using this reduced set. These values are then compared to the previous power and uncertainty measurements. If the new power is within one uncertainty of the previous power, it is assumed that the dropped face contributed nothing to the measurement. The process is then repeated by dropping another face, until the power is outside the uncertainty. The last power within the uncertainty is reported back to the program and used to calculate the DHR.

Both of these algorithms have been successfully implemented in IGAR and used to make measurements. The autotuning algorithm has been implemented and used

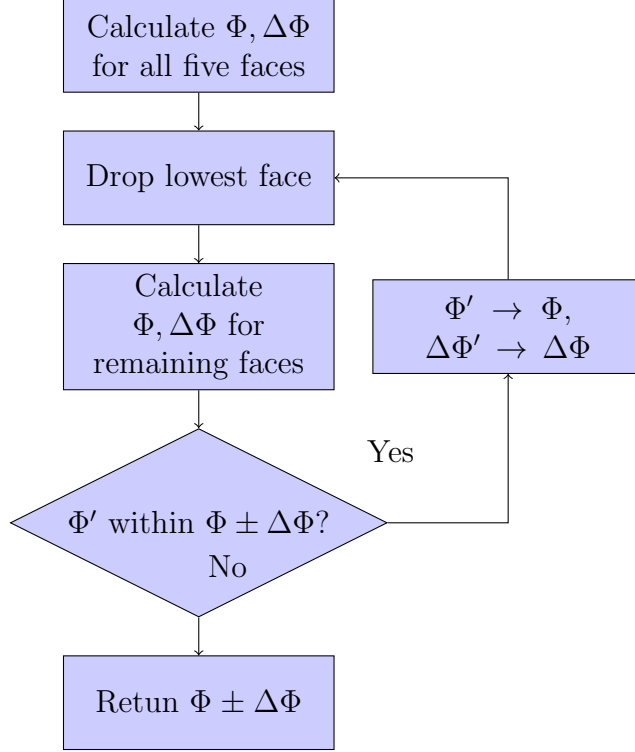


**Figure 21.** Algorithm for determining most accurate DHR from five sided detector.

successfully to make DHR measurements on a single sample at multiple wavelengths. For the samples examined in this paper, only a single wavelength was used, but IGAR has the capability of making multiple measurements automatically. The IGAR algorithm has been successfully used on all of the measurements shown in the next section. The outputs of this algorithm have been compared to the results without using the algorithm, and been shown that the algorithm decreases measurement uncertainty while retaining the accuracy of the DHR given the measured data.

## VIII. Measurements

IGAR has taken a number of measurements of different samples. Two of important note are an aluminum block with significant surface roughness and a measurement of the gold calibration mirror. The aluminum block is a sample with high reflectivity which is very diffuse. This means that the light reflected by the sample will be scattered over all five faces of the detector. The gold mirror is a much more specular sample, which will show the reflection walking over the detector.

For the following measurements, one of the QCLs was used to illuminate the sample. The laser was tuned to  $5.504\mu\text{m}$ . This particular laser emits vertically polarized light (parallel to the  $y$  axis), and no optics which affect polarization were used. Both of these measurements were taken using the same calibration data, which was taken slightly before the measurement.

### 8.1 Aluminum Block

The aluminum block is best compared to the Black Oxidized Steel scatterer shown in Section 4.5. While the samples have unequal DHR measurements, they both share a number of characteristics. Before continuing, we must address the peak at the end of the DHR measurement, seen in Figure 22. This peak occurs due to a misalignment of the incident laser beam. The fourth face of the detector could not be properly calibrated, which makes the contribution of this face to the DHR greater than it should be. Ignoring this error, the voltage seen by each face of the detector is very similar to what would be expected given a diffuse scatterer.

This is shown in Figure 23. While the Black Oxidized Steel scatterer is not completely accurate to the aluminum block, the signals across each face are consistent with each other. Face 2 seems to have the greatest discrepancy, but this is due to the

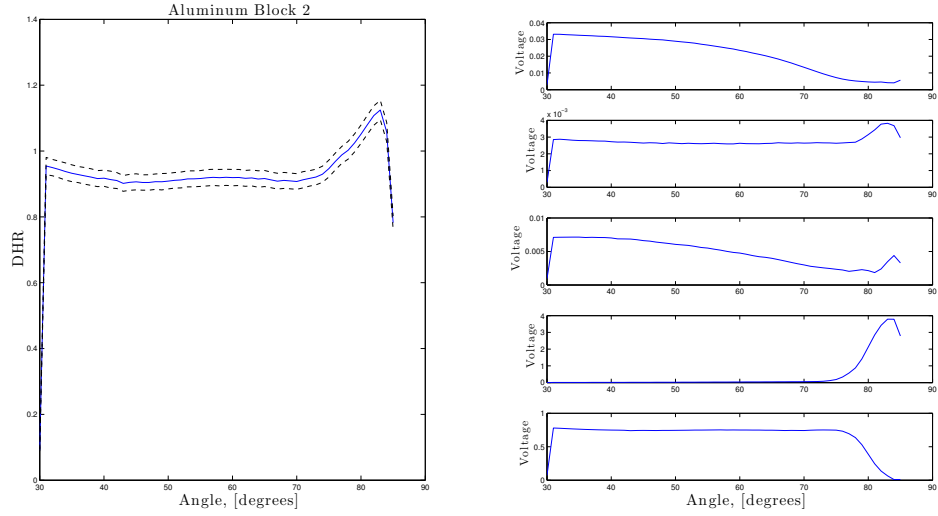


**Figure 22.** The DHR and face voltages for the rough surfaced aluminum block.

normalization. Examining Figure 22, this face has the lowest voltage of the five. The discrepancy in Figure 23 is due to poor normalization. The other four faces follow similar patterns to the Black Oxidized Steel scatterer. Faces 1 and 3 are the Left and Right faces, respectively, so it makes sense that the signal gradually drops off these faces as the sample approaches grazing angles. When this happens, the signal shift to the Front face (Face 4) of the detector, which happens in both measurements and the simulation.

With some further simulations, the aluminum scatterer could be more accurately modeled, and simulation could be made more accurate to what was measured in lab. Nonetheless, the correlation between the simulation of a diffuse scatterer and the measured data from IGAR shows that both systems work well in measuring DHR.

## 8.2 Gold Mirror

At first glance, the face measurements in Figure 25 do not appear consistent with one another. This is again, due to normalization. Faces 1, 2 and 3 have very little



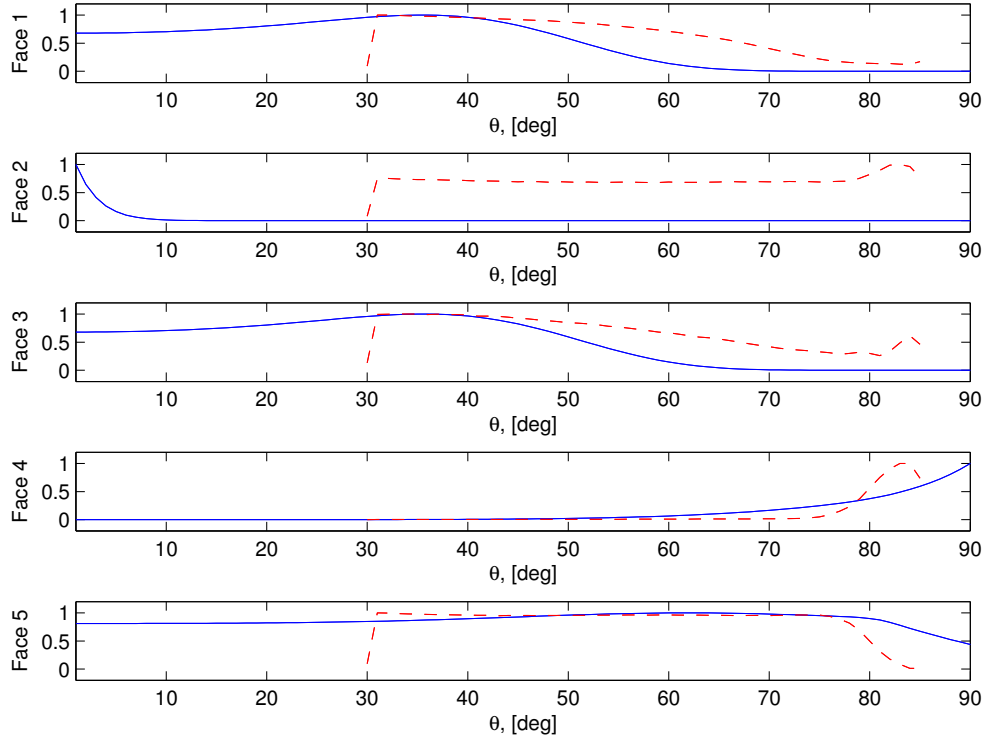


**Figure 23. Simulated measurements using the Black Oxidized Steel scatterer. Dashed red line is the voltage measurements of the rough aluminum block.**

signal compared to Faces 4 and 5. Because both the gold mirror and Gold Metallic scatterer are such specular samples, nearly all of the energy is concentrated on the front and top faces of the detector. The actual voltages can be seen in Figure 24. The numbers from the simulation are similarly low.

Faces 4 and 5 hold the most information in this sample. What is seen in Figure 25 is that the power reflected by the sample transition from the top face to the front face of the detector. This is seen happening gradually in the case of the Gold Metallic scatterer, and very quickly in the case of the gold mirror. This is mainly due to the construction of the simulation. In the simulation, the sample was square, and equally illuminated over its entire surface. For the measurement, the gold mirror was

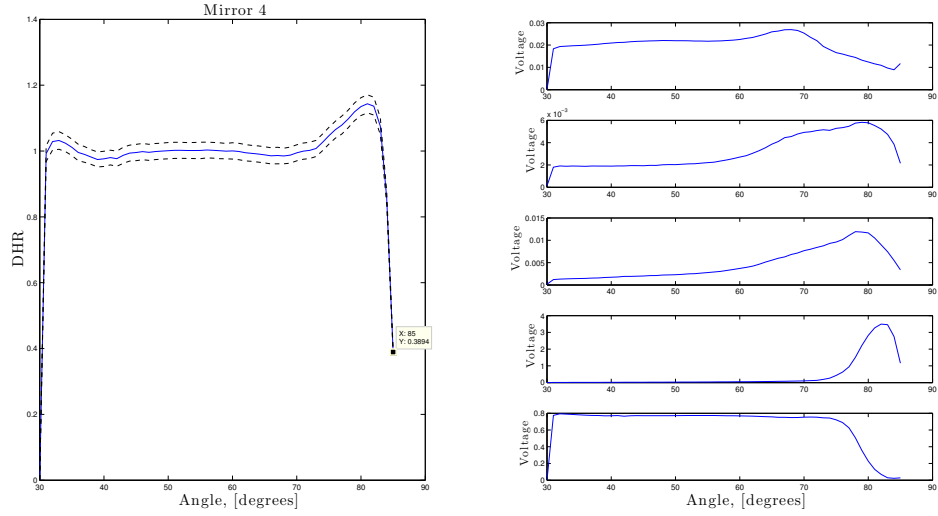


**Figure 24.** The DHR and face voltages for the gold calibration mirror.

illuminated by a Gaussian laser beam. This led to more power being concentrated at the middle of the beam, which explains the sudden dropoff between faces.

### 8.3 Experimental Results

These results show that the underlying theory of this experiment is accurate. The theoretical five-sided detector gives results that are similar to what can be measured in lab. The diffuse black oxidized steel scatterer gave results that very accurately resembled the aluminum block measured by IGAR. With a more accurate model, the simulated output of the system would be even closer to real results. Likewise, the gold scatterer followed the same patterns found in the gold mirror. Because both scatterers were highly specular, their results followed more closely, regardless of the inaccuracies of the underlying model. With some further time spent building models from measured BRDF, I am confident that the simulation of this system could even more closely resemble the experimental data.

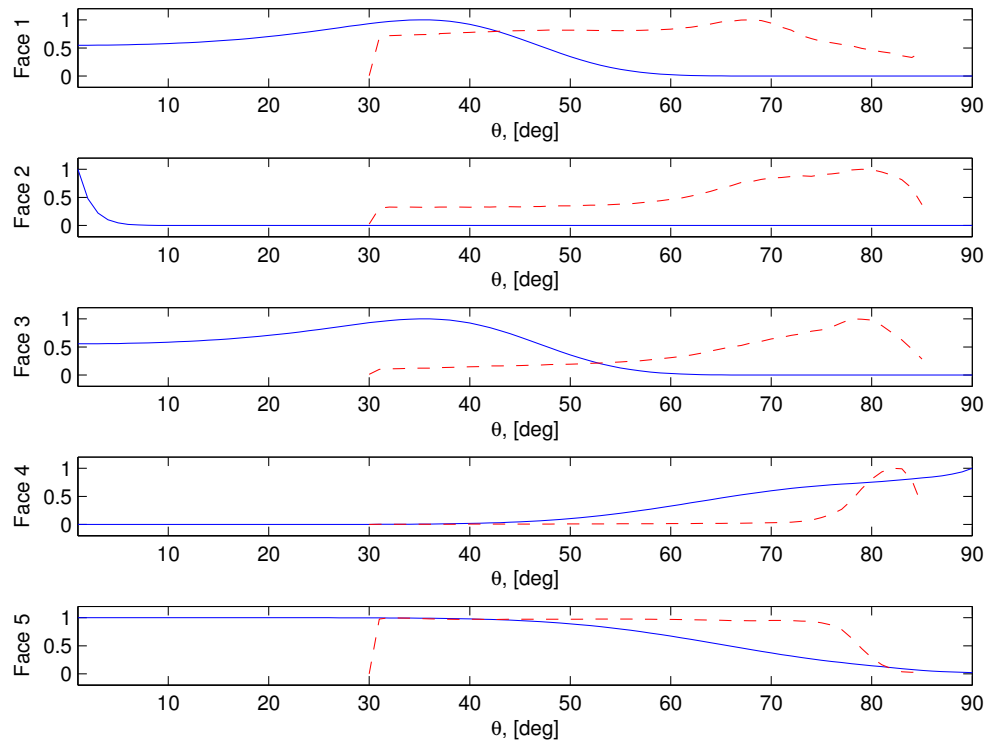


**Figure 25.** Simulated measurements using the Gold Metallic scatterer. Dashed red line is the voltage measurements of the gold calibration mirror.

## IX. Conclusions and Future Work

### 9.1 Conclusions

As our results have shown, IGAR can make measurements of the DHR of a sample. This ability stems from the design of the five sided pyroelectric detector. While the detector cannot capture all of the light reflected from the sample, the error of the measurement falls within the uncertainty of the sample, making this source of error negligible.

A robust calibration methodology ensures that the system makes accurate measurements. By carefully designing the system, the system can easily and accurately be calibrated. This calibration methodology has the added benefit of being able to be calibrated only knowing the exact characteristics of the calibration mirrors. All other elements of the system, such as the ratio of the beamsplitter or the voltage to power ratio of the detector faces can be calibrated out. This allows for high accuracy and ease of use.

Many of the errors found in the system can be traced back to the misalignment of the laser beam. With a better alignment procedure, many of these errors can be eliminated. Even so, the measurements taken by the system are promising. Many of the attributes found in the simulation of different scatterers can be backed up by experimental data. With more accurate scattering models, the experimentally collected data can be further verified.

IGAR shows much promise as a system capable of making DHR measurements at high angles of incidence. With its novel detector, tunable laser capabilities, and robust calibration procedures, it can make accurate measurements of DHR and increase the already impressive measurement capabilities of the United States Air Force.

## Appendix A. Measurement Uncertainty Expanded

In this appendix, we go from RD eqn whatever to RD 6.21. Eqn 6.21. Let's begin with

$$\rho(\theta) = \sum_{j=1}^5 C_{c,j} \frac{V_{d,j}(\theta)}{P_w} \quad (87)$$

Assuming the system is perfectly calibrated (i.e., there is no uncertainty in the calibration coefficient), there are three terms with uncertainties: uncertainty in the voltage measured at the detector ( $\Delta V_{d,j}$ ), power measured by the wavemeter ( $\Delta P_w$ ), and the uncertainty of the measurement of the DHR of the sample ( $\Delta \rho(\theta)$ ). Accounting for these uncertainties, the equation above becomes

$$\rho(\theta) + \Delta \rho(\theta) = \sum_{j=1}^5 C_{c,j} \frac{V_{d,j}(\theta) + \Delta V_{d,j}(\theta)}{P_w + \Delta P_w}. \quad (88)$$

Expanding the voltage term,

$$\rho(\theta) + \Delta \rho(\theta) = \sum_{j=1}^5 C_{c,j} \frac{V_{d,j}(\theta)}{P_w + \Delta P_w} + \sum_{j=1}^5 C_{c,j} \frac{\Delta V_{d,j}(\theta)}{P_w + \Delta P_w}. \quad (89)$$

Expanding the power term,

$$\begin{aligned} \rho(\theta) + \Delta \rho(\theta) &= \sum_{j=1}^5 C_{c,j} \frac{V_{d,j}(\theta)}{P_w} + \sum_{j=1}^5 C_{c,j} \frac{V_{d,j}(\theta)}{P_w^2} \Delta P_w \\ &\quad + \sum_{j=1}^5 C_{c,j} \frac{\Delta V_{d,j}(\theta)}{P_w} + \sum_{j=1}^5 C_{c,j} \frac{\Delta V_{d,j}(\theta)}{P_w^2} \Delta P_w. \end{aligned} \quad (90)$$

The uncertainty cross terms can be ignored. The term without any uncertainty is what was previously defined as the DHR of the measurement, and can be used to

cancel out the  $\rho(\theta)$  term. This leaves

$$\Delta\rho(\theta) = \sum_{j=1}^5 C_{c,j} \frac{V_{d,j}(\theta)}{P_w^2} \Delta P_w + \sum_{j=1}^5 C_{c,j} \frac{\Delta V_{d,j}(\theta)}{P_w}. \quad (91)$$

Using the definition of DHR, the equation can be further simplified down to

$$\Delta\rho(\theta) = \rho(\theta) \frac{\Delta P_w}{P_w} + \sum_{j=1}^5 C_{c,j} \frac{\Delta V_{d,j}(\theta)}{P_w}. \quad (92)$$

At this point, we see that even allowing uncertainty in calibration will not effect the uncertainty of the entire measurement. This uncertainty term is multiplied by the uncertainty of the voltage measurement, and can therefore be ignored.

Note that the first term is independent of face, while the second term is not. Because of this, ignoring the contributions of some of the faces can decrease the uncertainty of the measurement. This is the motivation for section whatever where we talk about the IGAR algorithm.

## Appendix B. MATLAB Code

Below is the MATLAB code used for the simulations found above in Chapter IV.  $\Phi_{\text{act}}$  is found by running code “cookTorrance”.  $\Phi_{\text{det}}$  is found running the code “detectorOptimal3”. Plots covering a range of angles were calculated by running this function over this angular range and plotting the results. “cookTorranceVL” functions the same as “cookTorrance”, but has input vector, as opposed to the angle of the incident light, and is called by “detectorOptimal3”.

### 2.1 cookTorrance.m

```
function [R,DHR] = cookTorrance(P,T)

if nargin < 2
    P = 45;
    T = 45;
end

% [sample name]      > F0      m
% acrylic blue       > 0.035   0.037
% black oxidized steel > 0.035   0.19
% black plastic soft > 0.136   0.325
% blue rubber        > 0.0366  0.276
% ball gold metallic 2 > 0.629   0.144
% ipswitch pine      > 0.0192  0.12
% metallic blue      > 0.638   0.231
% metallic silver    > 0.661   0.195
% nickel             > 0.733   0.0424
% provincial         > 0.114   0.0864
% red oak            > 0.0248  0.116

F0 = 0.629;      m = 0.144

n = (1+sqrt(F0))/(1-sqrt(F0));

p = 512;
[phi theta] = meshgrid(0:pi/2/p:pi/2, 0:2*pi/p:2*pi);

%% geometry calculations
```

```

[x y z] = sph2cart(theta,phi,ones(size(theta)));
V(1,::) = x;
V(2,::) = y;
V(3,::) = z;

L = [cosd(P)*cosd(T) sind(P)*cosd(T) sind(T)];
Lp(1,::) = L(1)*ones(size(V(1,::)));
Lp(2,::) = L(2)*ones(size(V(1,::)));
Lp(3,::) = L(3)*ones(size(V(1,::)));

temp = V + Lp;
H1 = sqrt(temp(1,::).^2 + temp(2,::).^2 + temp(3,::).^2);
H(1,::) = temp(1,::)/H1;
H(2,::) = temp(2,::)/H1;
H(3,::) = temp(3,::)/H1;
cosTheta = V(1,::).*H(1,::) + V(2,::).*H(2,::) + V(3,::).*H(3,::);

%% cook-torrance constants

cosDelta = H(3,::);
sinDelta = sqrt(1-H(3,::).^2);
tanDelta = sinDelta./cosDelta;
D = 1/m^2/cosDelta.^4.*exp(-(tanDelta/m).^2);

Gp(1,::) = ones(size(V(1,::)));
Gp(2,::) = 2*H(3,::).*V(3,::)/cosTheta;
Gp(3,::) = 2*H(3,::).*Lp(3,::)/cosTheta;
G = min(Gp,[],1);

%% fresnel calculations

n = 10.39993 + i*40;
g = sqrt(n^2 + cosTheta.^2 -1);
F = 1/2*(g-cosTheta).^2./(g+cosTheta).^2
    .*(1 + (cosTheta.*(g+cosTheta) - 1).^2
    ./((cosTheta.*(g-cosTheta) + 1).^2);

%% cook-torrance calculations

K = 1/pi*D.*G./Lp(3,::)/V(3,::).*F;

if 1

```



```

    %[x y z] = sph2cart(theta,phi,ones(size(theta)));
    surf(x,y,z,squeeze(abs(K)), 'EdgeAlpha',0)
    %surf(x,y,z,z, 'EdgeAlpha',0)
    axis equal
    axis([-1 1 -1 1 -0 1]*1.2)
end

nanFinder = isnan(K);
S = size(K);
for j = 1:S(1)
    for k = 1:S(2)
        if nanFinder(j,k) == 1
            K(j,k) = 0;
        end
    end
end
R = squeeze(K);

DHR = sum(sum(R*pi/p*pi/p*4.*sin(pi/2-phi).*cos(pi/2-phi)));

if nargin < 2
    R = 0; DHR = 0;
end

end

```

## 2.2 cookTorranceVL.m

```

function [R] = cookTorranceVL(V,Lp)

% [sample name]      > F0      m
% black plastic soft  > 0.136   0.325
% blue rubber         > 0.0366  0.276
% ball gold metllic 2 > 0.629   0.144
% ipswitch pine       > 0.0192  0.12
% metallic blue       > 0.638   0.231
% metallic silver     > 0.661   0.195
% nickel              > 0.733   0.0424
% provincial           > 0.114   0.0864
% red oak              > 0.0248  0.116

F0 = 0.661; m = 0.195;

```

```

n = (1+sqrt(F0))/(1-sqrt(F0));

%% geometry calculations

V1 = sqrt(V(1,::).^2 + V(2,::).^2 + V(3,::).^2);
V(1,::) = V(1,::)/V1;
V(2,::) = V(2,::)/V1;
V(3,::) = V(3,::)/V1;

L1 = sqrt(Lp(1,::).^2 + Lp(2,::).^2 + Lp(3,::).^2 );
Lp(1,::) = Lp(1,::)/L1;
Lp(2,::) = Lp(2,::)/L1;
Lp(3,::) = Lp(3,::)/L1;

temp = V + Lp;
H1 = sqrt(temp(1,::).^2 + temp(2,::).^2 + temp(3,::).^2);
H(1,::) = temp(1,::)/H1;
H(2,::) = temp(2,::)/H1;
H(3,::) = temp(3,::)/H1;
cosTheta = V(1,::).*H(1,::) + V(2,::).*H(2,::) + V(3,::).*H(3,::);

%% cook-torrance constants

cosDelta = H(3,::);
sinDelta = sqrt(1-H(3,::).^2);
tanDelta = sinDelta./cosDelta;
D = 1/m^2/cosDelta.^4.*exp(-(tanDelta/m).^2);

Gp(1,::) = ones(size(V(1,::)));
Gp(2,::) = 2*H(3,::).*V(3,::)/cosTheta;
Gp(3,::) = 2*H(3,::).*Lp(3,::)/cosTheta;
G = min(Gp,[],1);

%% fresnel calculations

g = sqrt(n^2 + cosTheta.^2 -1);
F = 1/2*(g-cosTheta).^2./(g+cosTheta).^2
    .*(1 + (cosTheta.*(g+cosTheta) - 1).^2
    ./((cosTheta.*(g-cosTheta) + 1).^2);

%% cook-torrance calculations

```

```

K = 1/pi*D.*G./Lp(3, :, :)./V(3, :, :).*F;

if 0
    [x y z] = sph2cart(theta, phi, ones(size(theta)));
    surf(x, y, z, squeeze(abs(D)), 'EdgeAlpha', 0)
    axis vis3d
    axis([-2 2 -2 2 0 2])
end

nanFinder = isnan(K);
S = size(K);
for j = 1:S(1)
    for k = 1:S(2)
        if nanFinder(j, k) == 1
            K(j, k) = 0;
        end
    end
end

R = K; %squeeze(F);

%DHR = sum(sum(R*pi/p*pi/p*4.*sin(pi/2-phi).*cos(pi/2-phi)));

end

```

### 2.3 detectorOptimal3.m

```

function [S, PhiVec, PhiStruct] = detectorOptimal3(theta, phi)

if nargin < 1
    theta = 35;
end
if nargin < 2
    phi = 0;
end

%% definitions

n1 = 1; n2 = 4;

xEMax = 1/2; % 1/2 width
dxE = 0.1;
yEMax = 1/2; % 1/2 width

```

```

dyE = 0.1;

xDMax = 10; % 1/2 width
dxD = 0.1/1;
yDMax = 20; % 1/2 width <- longer dimension
dyD = 0.1/1;
zDMax = 10; % full height
dzD = 0.1/1;

[xe ye] = meshgrid(-xEMax:dxE:xEMax, -yEMax:dyE:yEMax);

Lo = [cosd(theta)*cosd(phi) cosd(theta)*sind(phi) sind(theta)];
N = [0 0 1];

%% top face
% z held constant, integrate over x and y

t = []; f = []; l = [];
[t.xd t.yd] = meshgrid(-xDMax:dxD:xDMax, -yDMax:dyD:yDMax);
[f.yd f.zd] = meshgrid(-yDMax:dyD:yDMax, 0+0.0001:dzD:zDMax);
[l.xd l.zd] = meshgrid(-xDMax:dxD:xDMax, 0+0.0001:dzD:zDMax);

S = size(xe);
PhiTop = zeros(size(t.xd));
PhiFront = zeros(size(f.yd));
PhiLeft = zeros(size(l.xd));
PhiBack = zeros(size(f.yd));
PhiRight = zeros(size(l.xd));

if 1
for K = 1:S(1)
    for L = 1:S(2)
        if (abs(xe(K,L)) < xDMax) && (abs(ye(K,L)) < yDMax)
            Ve = [xe(K,L) ye(K,L) 0];

            %% top face
            clear V Vd Lp
            Vd(1, :, :) = t.xd;
            Vd(2, :, :) = t.yd;
            Vd(3, :, :) = zDMax*ones(size(t.xd));

            V(1, :, :) = Vd(1, :, :) - Ve(1);
            V(2, :, :) = Vd(2, :, :) - Ve(2);

```

```

V(3, :, :) = Vd(3, :, :) - Ve(3);

Lp(1, :, :) = Lo(1)*ones(size(V(1, :, :)));
Lp(2, :, :) = Lo(2)*ones(size(V(1, :, :)));
Lp(3, :, :) = Lo(3)*ones(size(V(1, :, :)));

R = sqrt(V(1, :, :).^2 + V(2, :, :).^2 + V(3, :, :).^2);
cosThetaE = V(3, :, :)./R;
cosThetaD = V(3, :, :)./R;
A = reflection(n1,n2,cosThetaD);

I = cookTorranceVL(V,Lp);
Lr = A.*I.*cosThetaE;
PhiTop = PhiTop + squeeze(Lr.*A.*cosThetaD
    .*1./R.^2*dxE*dyE*dxD*dyD);

%% front face
clear V Vd Lp
Vd(1, :, :) = xDMax*ones(size(f.yd));
Vd(2, :, :) = f.yd;
Vd(3, :, :) = f.zd;

V(1, :, :) = Vd(1, :, :) - Ve(1);
V(2, :, :) = Vd(2, :, :) - Ve(2);
V(3, :, :) = Vd(3, :, :) - Ve(3);

VFront = V;

Lp(1, :, :) = Lo(1)*ones(size(V(1, :, :)));
Lp(2, :, :) = Lo(2)*ones(size(V(1, :, :)));
Lp(3, :, :) = Lo(3)*ones(size(V(1, :, :)));

R = sqrt(V(1, :, :).^2 + V(2, :, :).^2 + V(3, :, :).^2);
cosThetaE = V(3, :, :)./R;
cosThetaD = V(1, :, :)./R;
A = reflection(n1,n2,cosThetaD);
I = cookTorranceVL(V,Lp);
Lr = A.*I.*cosThetaE;
PhiFront = PhiFront + squeeze(Lr.*A.*cosThetaD
    .*1./R.^2*dxE*dyE*dyD*dzD);

%% left face
clear V Vd Lp

```

```

Vd(1, :, :) = l.xd;
Vd(2, :, :) = yDMax*ones(size(l.xd));
Vd(3, :, :) = l.zd;

V(1, :, :) = Vd(1, :, :) - Ve(1);
V(2, :, :) = Vd(2, :, :) - Ve(2);
V(3, :, :) = Vd(3, :, :) - Ve(3);

Lp(1, :, :) = Lo(1)*ones(size(V(1, :, :)));
Lp(2, :, :) = Lo(2)*ones(size(V(1, :, :)));
Lp(3, :, :) = Lo(3)*ones(size(V(1, :, :)));

R = sqrt(V(1, :, :).^2 + V(2, :, :).^2 + V(3, :, :).^2);
cosThetaE = V(3, :, :)./R;
cosThetaD = V(2, :, :)./R;
A = reflection(n1,n2,cosThetaD);
I = cookTorranceVL(V,Lp);
Lr = A.*I.*cosThetaE;
PhiLeft = PhiLeft + squeeze(Lr.*A.*cosThetaD
    .*1./R.^2*dxE*dyE*dxD*dzD);

%% back face
clear V Vd Lp
Vd(1, :, :) = -xDMax*ones(size(f.yd));
Vd(2, :, :) = f.yd;
Vd(3, :, :) = f.zd;

V(1, :, :) = Vd(1, :, :) - Ve(1);
V(2, :, :) = Vd(2, :, :) - Ve(2);
V(3, :, :) = Vd(3, :, :) - Ve(3);

VBack = V;

Lp(1, :, :) = Lo(1)*ones(size(V(1, :, :)));
Lp(2, :, :) = Lo(2)*ones(size(V(1, :, :)));
Lp(3, :, :) = Lo(3)*ones(size(V(1, :, :)));

R = sqrt(V(1, :, :).^2 + V(2, :, :).^2 + V(3, :, :).^2);
cosThetaE = V(3, :, :)./R;
cosThetaD = -V(1, :, :)./R;
A = reflection(n1,n2,cosThetaD);
I = cookTorranceVL(V,Lp);
Lr = A.*I.*cosThetaE;

```

```

PhiBack = PhiBack + squeeze(Lr.*A.*cosThetaD
    .*1./R.^2*dxE*dyE*dyD*dzD);

%% right face
clear V Vd Lp
Vd(1, :, :) = l.xd;
Vd(2, :, :) = -yDMax*ones(size(l.xd));
Vd(3, :, :) = l.zd;

V(1, :, :) = Vd(1, :, :) - Ve(1);
V(2, :, :) = Vd(2, :, :) - Ve(2);
V(3, :, :) = Vd(3, :, :) - Ve(3);

Lp(1, :, :) = Lo(1)*ones(size(V(1, :, :)));
Lp(2, :, :) = Lo(2)*ones(size(V(1, :, :)));
Lp(3, :, :) = Lo(3)*ones(size(V(1, :, :)));

R = sqrt(V(1, :, :).^2 + V(2, :, :).^2 + V(3, :, :).^2);
cosThetaE = V(3, :, :)./R;
cosThetaD = -V(2, :, :)./R;
A = reflection(n1,n2,cosThetaD);
I = cookTorranceVL(V,Lp);
Lr = A.*I.*cosThetaE;
PhiRight = PhiRight + squeeze(Lr.*A.*cosThetaD
    .*1./R.^2*dxE*dyE*dxD*dzD);

end
end

disp(['Completed: ' num2str(K/S(1)*100,'%0.4g') ])
end

PhiVec = [sum(sum(PhiTop)); sum(sum(PhiLeft));
    sum(sum(PhiFront)); sum(sum(PhiRight)); sum(sum(PhiBack)) ];

PhiStruct=[];
PhiStruct.PT = PhiTop;
PhiStruct.PL = PhiLeft;
PhiStruct.PF = PhiFront;
PhiStruct.PR = PhiRight;
PhiStruct.PB = PhiBack;
PhiStruct.VBack = VBack;
PhiStruct.VFront = VFront;

```

```

m(1) = max(max(PhiTop));
m(2) = max(max(PhiLeft));
m(3) = max(max(PhiFront));
m(4) = max(max(PhiRight));
m(5) = max(max(PhiBack));
M = 1;

if 0
    figure(1)
    subplot(3,3,5)
    image(rot90(PhiTop,1)/M*64); title('top'); axis image
    subplot(3,3,4)
    image(rot90(PhiLeft,3)/M*64); title('left'); axis image
    subplot(3,3,2)
    image(rot90(PhiFront,4)/M*64); title('front'); axis image
    subplot(3,3,6)
    image(rot90(PhiRight,1)/M*64); title('right'); axis image
    subplot(3,3,8)
    image(rot90(PhiBack,2)/M*64); title('back'); axis image
    %figure
    %image(squeeze(IPrime))
end
if 1
    a = size(PhiLeft);
    b = size(PhiFront);
    It = [-1*ones(a(1), b(1)) fliplr(PhiFront)/M -1*ones(a(1),
        b(1))];
    Im = [rot90(PhiLeft,1)/M fliplr(rot90(PhiTop,1))/M
        fliplr(rot90(PhiRight,1))/M];
    Ib = [-1*ones(a(1), b(1)) fliplr(flipud(PhiBack))/M -1*ones(a(1),
        b(1))];
    I = [It; Im; Ib];
    figure(2)
    PhiStruct.Image = I;
    imagesc(rot90(PhiStruct.Image))
    axis image;
end

pC = sum(sum(PhiTop)) + sum(sum(PhiLeft)) + sum(sum(PhiFront))
    + sum(sum(PhiRight)) + sum(sum(PhiBack));
pE = pi*2*xEMax*2*yEMax;

```



```

eta = pC/pE;
%figure(1)
%subplot(3,3,9);
[R,DHR] = cookTorrance(45,theta);
S = eta/DHR

PhiStruct.xE = xe;
PhiStruct.yE = ye;

end

end

function [A Rt Rs Rp] = reflection(n1, n2, cosTheta)

sinTheta = sqrt(1 - cosTheta.^2);

Rs = abs( (n1*cosTheta - n2*sqrt(1 - n1/n2*sinTheta))
          ./ (n1*cosTheta + n2*sqrt(1 - n1/n2*sinTheta)) ).^2;
Rt = abs( (n1*sqrt(1-n1/n2*sinTheta) - n2*cosTheta)
          ./ (n1*sqrt(1-n1/n2*sinTheta) + n2*cosTheta) ).^2;
Rp = (Rs+Rt)/2;
A = 1-Rp;

end

```

## Bibliography

- [1] Addy Ngan, Wojciech Matsusik, Fredo Durand. “Experimental Analysis of BRDF Models - Supplemental”. *Eurographics Symposium on Rendering*, 2005.
- [2] Balling, Bradley. *A Comparative Study of the Bidirectional Reflectance Distribution Function of Several Surfaces as a Mid-wave Infrared Diffuse Reflectance Standard*. Master’s thesis, Air Force Institute of Technology, 2009.
- [3] Bartell, FO, EL Dereniak, and WL Wolfe. “The theory and measurement of bidirectional reflectance distribution function/BRDF/and bidirectional transmittance distribution function/BTDF”. *Society of Photo-Optical Instrumentation Engineers (SPIE) Conference Series*, volume 257, 154–160. 1981.
- [4] Blinn, James F. “Models of Light Reflection For Computer Synthesized Pictures”. *Siggraph*, 77.
- [5] Company, Access Laser. *Lasy4g Operator Manual*.
- [6] Corporation, Northrop Grumman. *Infrared Grazing Angle Reflectometer User Manual*.
- [7] Corporation, Northrop Grumman. *Infrared Grazing Angle Reflectometer (IGAR) Introduction*. Technical report, Northrop Grumman, 2011.
- [8] E. L. Dereniak, G. D. Boreman. *Infrared Detectors and Systems*. John Wiley and Sons, Inc., 1996.
- [9] Eismann, Michael T. *Hyperspectral Remote Sensing*, volume PM210. SPIE Press, 2012.
- [10] Hecht, Eugene. *Optics*. Addison Wesley Publishing Company, 1997.
- [11] Instruments, Bristol. *Laser Spectrum Analyzer 721 Series*.
- [12] Lawrence B. Wolff, Michael Oren, Shree K. Nayar. “Improved Diffuse Reflection Models for Computer Vision”. *International Journal of Computer Vision*, 30, 1998.
- [13] Nicodemus, F. E. “Reflectance Nomenclature and Directional Reflectance and Emissivity”. *Applied Optics*, 9(6), June 1970.
- [14] Nicodemus, Fred E. *Directional Reflectance and Emissivity of an Opaque Surface*. Technical report, Electronic Defense Laboratories, 1965.
- [15] Robert L. Cook, Kenneth E. Torrance. “A Reflectance Model for Computer Graphics”. *ACM Transactions on Graphics*, 1(1):7–24, January 1982.

- [16] Robert L. Cook, Kenneth E. Torrance. “A Reflectance Model for Computer Graphics”. *ACM Transactions on Graphics*, 1(1):7–24, January 1982.
- [17] Solutions, Daylight. *Model TLS-21XX Tunable QCL Controller CW/Pulsed User Manual*.
- [18] of Standards, United States. National Bureau and F.E. Nicodemus. *Geometrical Considerations and Nomenclature for Reflectance*. US Department of Commerce, National Bureau of Standards, 1977.

## **Vita**

Michael Benson was born in Bryn Mawr, Pennsylvania. After graduation from Whitinsville Christian School in 2006, he went to study Electrical Engineering at Cedarville University. Upon graduating in the Spring of 2010, he went on to work as a research assistant under Dr. Marciniak at the Air Force Institute of Technology, located on the Wright Patterson Air Force Base of Ohio. During this time, he worked towards a Master's Degree in Optical Sciences and Engineering. After this, he will continue his education pursuing a Doctorate in Optical Sciences and Engineering.

# REPORT DOCUMENTATION PAGE

Form Approved  
OMB No. 0704-0188

The public reporting burden for this collection of information is estimated to average 1 hour per response, including the time for reviewing instructions, searching existing data sources, gathering and maintaining the data needed, and completing and reviewing the collection of information. Send comments regarding this burden estimate or any other aspect of this collection of information, including suggestions for reducing this burden to Department of Defense, Washington Headquarters Services, Directorate for Information Operations and Reports (0704-0188), 1215 Jefferson Davis Highway, Suite 1204, Arlington, VA 22202-4302. Respondents should be aware that notwithstanding any other provision of law, no person shall be subject to any penalty for failing to comply with a collection of information if it does not display a currently valid OMB control number. **PLEASE DO NOT RETURN YOUR FORM TO THE ABOVE ADDRESS.**

<b>1. REPORT DATE (DD-MM-YYYY)</b> 14-06-2012			<b>2. REPORT TYPE</b> Master's Thesis		<b>3. DATES COVERED (From — To)</b> Nov 2010 – Jun 2012	
<b>4. TITLE AND SUBTITLE</b>  Characterization and Measurements from the Infrared Grazing Angle Reflectometer					<b>5a. CONTRACT NUMBER</b>	
					<b>5b. GRANT NUMBER</b>	
					<b>5c. PROGRAM ELEMENT NUMBER</b>	
<b>6. AUTHOR(S)</b>  Benson, Michael R.					<b>5d. PROJECT NUMBER</b>	
					<b>5e. TASK NUMBER</b>	
					<b>5f. WORK UNIT NUMBER</b>	
<b>7. PERFORMING ORGANIZATION NAME(S) AND ADDRESS(ES)</b> Air Force Institute of Technology Graduate School of Engineering and Management (AFIT/EN) 2950 Hobson Way WPAFB OH 45433-7765					<b>8. PERFORMING ORGANIZATION REPORT NUMBER</b>  AFIT/OSE/ENP/12-J01	
<b>9. SPONSORING / MONITORING AGENCY NAME(S) AND ADDRESS(ES)</b>  intentionally left blank					<b>10. SPONSOR/MONITOR'S ACRONYM(S)</b>	
					<b>11. SPONSOR/MONITOR'S REPORT NUMBER(S)</b>	
<b>12. DISTRIBUTION / AVAILABILITY STATEMENT</b>  This material is declared a work of the U.S. Government and is not subject to copyright protection in the United States.						
<b>13. SUPPLEMENTARY NOTES</b>						
<b>14. ABSTRACT</b>  A commonly used metric for measuring the reflective properties of a sample is Directional Hemispherical Reflectance (DHR). The Infrared Grazing Angle Reflectometer measures DHR at high angles of incidence. To facilitate this measurement, a novel three dimensional multi-face pyroelectric detector is used. This detector can theoretically measure better than 98% of the light reflected by the sample, regardless of the diffusivity of the sample measured. The setup of this equipment is discussed, and the procedure for calibration is derived. Several of the difficulties in performing measurements are described, and several sample measurements are discussed.						
<b>15. SUBJECT TERMS</b>  Directional Hemispherical Reflectance, Infrared Grazing Angle Reflectometer, five sided detector, pyroelectric, hemi-ellipsoidal mirror						
<b>16. SECURITY CLASSIFICATION OF:</b>			<b>17. LIMITATION OF ABSTRACT</b>	<b>18. NUMBER OF PAGES</b>	<b>19a. NAME OF RESPONSIBLE PERSON</b>	
<b>a. REPORT</b>	<b>b. ABSTRACT</b>	<b>c. THIS PAGE</b>			Michael A. Marciniak, AFIT/ENP	
U	U	U	UU	79	<b>19b. TELEPHONE NUMBER (include area code)</b> (937) 255-3636 x4529	